

See discussions, stats, and author profiles for this publication at: <https://www.researchgate.net/publication/11036435>

# Spectroscopic and computational studies on $[(\text{PhTt}(\text{tBu}))_2\text{Ni}_2(\mu\text{-O})_2]$ : nature of the bis- $\mu\text{-oxo}$ $(\text{Ni}^{3+})_2$ diamond core.

ARTICLE in JOURNAL OF THE AMERICAN CHEMICAL SOCIETY · NOVEMBER 2002

Impact Factor: 12.11 · Source: PubMed

CITATIONS

7

READS

20

## 4 AUTHORS, INCLUDING:



**Charles G Riordan**

University of Delaware

81 PUBLICATIONS 1,881 CITATIONS

SEE PROFILE



**Thomas C Brunold**

University of Wisconsin–Madison

102 PUBLICATIONS 3,908 CITATIONS

SEE PROFILE

## Spectroscopic and Computational Studies on [(PhTt<sup>tBu</sup>)<sub>2</sub>Ni<sub>2</sub>(μ-O)<sub>2</sub>]: Nature of the Bis-μ-oxo (Ni<sup>3+</sup>)<sub>2</sub> “Diamond” Core

Ralph Schenker,<sup>†</sup> Beaven S. Mandimutsira,<sup>‡</sup> Charles G. Riordan,<sup>‡</sup> and  
Thomas C. Brunold<sup>\*†</sup>

*Contribution from the Department of Chemistry, University of Wisconsin–Madison,  
Madison, Wisconsin 53706, and the Department of Chemistry and Biochemistry,  
University of Delaware, Newark, Delaware 19716*

Received May 25, 2002

**Abstract:** Spectroscopic and density functional theory (DFT) electronic structure computational studies on a binuclear bis-μ-oxo bridged (Ni<sup>3+</sup>)<sub>2</sub> complex, [(PhTt<sup>tBu</sup>)<sub>2</sub>Ni<sub>2</sub>(μ-O)<sub>2</sub>] (**1**), where (PhTt<sup>tBu</sup>) represents phenyltris((*tert*-butylthio)methyl)borate, are presented and discussed. These studies afford a detailed description of the Ni<sub>2</sub>O<sub>2</sub> core electronic structure in bis-μ-oxo (Ni<sup>3+</sup>)<sub>2</sub> dimers and provide insight into the possible role of the (PhTt<sup>tBu</sup>) thioether ligand in the formation of **1** from a Ni<sup>1+</sup> precursor by O<sub>2</sub> activation. From a normal coordinate analysis of resonance Raman data, a value of  $k_{\text{Ni-O}} = 2.64 \text{ mdyn/Å}$  is obtained for the Ni–O stretch force constant for **1**. This value is smaller than  $k_{\text{Cu-O}} = 2.82\text{--}2.90 \text{ mdyn/Å}$  obtained for bis-μ-oxo (Cu<sup>3+</sup>)<sub>2</sub> dimers possessing nitrogen donor ligands, indicating a reduced metal–oxo bond strength in **1**. Electronic absorption and magnetic circular dichroism spectroscopic techniques permit identification of several O→Ni and S→Ni charge transfer (CT) transitions that are assigned on the basis of DFT calculations. The dominant O→Ni CT transition of **1** occurs at 17 700 cm<sup>−1</sup>, red-shifted by ~7000 cm<sup>−1</sup> relative to the corresponding transition in bis-μ-oxo (Ni<sup>3+</sup>)<sub>2</sub> dimers with nitrogen donor ligands. This red-shift along with the relatively low value of  $k_{\text{Ni-O}}$  are due primarily to the presence of the thioether ligands in **1** that greatly affect the compositions of the Ni<sub>2</sub>O<sub>2</sub> core MOs. This unique property of the thioether ligand likely contributes to the reactivity of the Ni center in the precursor [(PhTt<sup>tBu</sup>)Ni<sup>1+</sup>CO] toward O<sub>2</sub>. DFT computations reveal that conversion of a hypothetical side-on peroxo (Ni<sup>2+</sup>)<sub>2</sub> dimer, [(PhTt<sup>tBu</sup>)<sub>2</sub>Ni<sub>2</sub>(μ-η<sup>2</sup>:η<sup>2</sup>-O<sub>2</sub>)], to the bis-μ-oxo (Ni<sup>3+</sup>)<sub>2</sub> dimer **1** is energetically favorable by 32 kcal/mol and occurs without a significant activation energy barrier ( $\Delta H^\ddagger = 2 \text{ kcal/mol}$ ).

### 1. Introduction

Understanding the mechanisms of O<sub>2</sub> and H<sub>2</sub>O<sub>2</sub> activation by transition metal complexes is of great fundamental and practical interest. This type of reaction has been shown to afford high-valent bis-μ-oxo bridged dimers that possess a M<sub>2</sub>(μ-O)<sub>2</sub> (M = Cu,<sup>1–3</sup> Fe,<sup>1,4</sup> Co,<sup>5</sup> and Ni<sup>5–7</sup>) “diamond” core structure. These thermally unstable complexes are capable of performing diverse organic functionalizations by means of intra- or intermolecular oxidative C–H abstraction and thus possess tremendous potential for use as oxidation catalysts. Additionally, the copper and iron complexes have recently attracted attention as models of possible reaction intermediates of O<sub>2</sub> activating enzymes such as the Cu proteins tyrosinase<sup>8,9</sup> and catechol

oxidase<sup>10</sup> and the Fe proteins methane monooxygenase (intermediate Q)<sup>11–13</sup> and ribonucleotide reductase (intermediate X).<sup>11,12,14</sup>

- (3) (a) Mahapatra, S.; Halfen, J. A.; Wilkinson, E. C.; Pan, G.; Cramer, C. J.; Que, L., Jr.; Tolman, W. B. *J. Am. Chem. Soc.* **1995**, *117*, 8865. (b) Mahapatra, S.; Young, V. G., Jr.; Tolman, W. B. *Angew. Chem.* **1997**, *109*, 125; *Angew. Chem., Int. Ed. Engl.* **1997**, *36*, 130. (c) Mahadevan, V.; Hou, Z.; Cole, A. P.; Root, D. E.; Lal, T. K.; Solomon, E. I.; Stack, T. D. P. *J. Am. Chem. Soc.* **1997**, *119*, 11996. (d) Holland, P. L.; Rodgers, K. R.; Tolman, W. B. *Angew. Chem.* **1999**, *111*, 1210; *Angew. Chem., Int. Ed. Engl.* **1999**, *38*, 1139. (e) Enomoto, M.; Aida, T. *J. Am. Chem. Soc.* **1999**, *121*, 874. (f) Mahadevan, V.; DuBois, J. L.; Hedman, B.; Hodgson, K. O.; Stack, T. D. P. *J. Am. Chem. Soc.* **1999**, *121*, 5583. (g) Straub, B. F.; Rominger, F.; Hofmann, P. *Chem. Commun.* **2000**, 1611. (h) Funahashi, Y.; Nakaya, K.; Hirota, S.; Yamauchi, O. *Chem. Lett.* **2000**, 1172. (i) Spencer, D. J. E.; Aboelallaa, N. W.; Reynolds, A. M.; Holland, P. L.; Tolman, W. B. *J. Am. Chem. Soc.* **2002**, *124*, 2108.
- (4) (a) Zang, Y.; Dong, Y.; Que, L., Jr.; Kauffmann, K.; Münck, E. *J. Am. Chem. Soc.* **1995**, *117*, 1169. (b) Dong, Y.; Fujii, H.; Hendrich, M. P.; Leising, R. A.; Pan, G.; Randall, C. R.; Wilkinson, E. C.; Zang, Y.; Que, L., Jr.; Fox, B. G.; Kauffmann, K.; Münck, E. *J. Am. Chem. Soc.* **1995**, *117*, 2778. (c) Dong, Y.; Que, L., Jr.; Kauffmann, K.; Münck, E. *J. Am. Chem. Soc.* **1995**, *117*, 11377. (d) Dong, Y.; Zang, Y.; Shu, L.; Wilkinson, E. C.; Kauffmann, K.; Münck, E.; Que, L., Jr. *J. Am. Chem. Soc.* **1997**, *119*, 12683. (e) Kim, C.; Dong, Y.; Que, L., Jr. *J. Am. Chem. Soc.* **1997**, *119*, 3635. (f) Hsu, H.-F.; Dong, Y.; Shu, L.; Young, V. G., Jr.; Que, L., Jr. *J. Am. Chem. Soc.* **1999**, *121*, 5230. (g) Zheng, H.; Zang, Y.; Dong, Y.; Young, V. G., Jr.; Que, L., Jr. *J. Am. Chem. Soc.* **1999**, *121*, 2226. (h) Costas, M.; Rohde, J.-U.; Stubna, A.; Ho, R. Y. N.; Quaroni, L.; Münck, E.; Que, L., Jr. *J. Am. Chem. Soc.* **2001**, *123*, 12931.

\* Address correspondence to this author. Fax: (608)262-6143; e-mail: brunold@chem.wisc.edu.

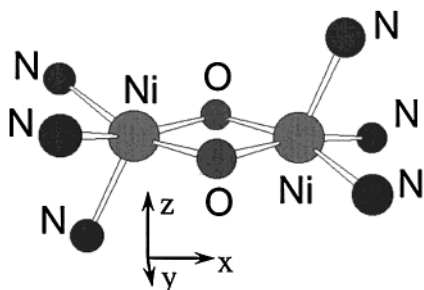
<sup>†</sup> University of Wisconsin–Madison.

<sup>‡</sup> University of Delaware.

(1) For a recent review, see: Que, L., Jr.; Tolman, W. B. *Angew. Chem., Int. Ed.* **2002**, *41*, 1114.

(2) Mahapatra, S.; Halfen, J. A.; Wilkinson, E. C.; Pan, G.; Wang, X.; Young, V. G., Jr.; Cramer, C. J.; Que, L., Jr.; Tolman, W. B. *J. Am. Chem. Soc.* **1996**, *118*, 11555.

Chart 1



A detailed understanding of the reaction mechanisms by which high-valent bis- $\mu$ -oxo dimers are formed and of the factors that influence their reactivity are of paramount interest. As particular emphasis has been placed on copper complexes, a large number of different bis- $\mu$ -oxo ( $\text{Cu}^{3+}$ )<sub>2</sub> dimers with a great variety of nitrogen supporting ligands have been reported.<sup>3</sup> Stopped-flow kinetic studies have provided significant insight into the mechanism of  $\text{O}_2$  activation by  $\text{Cu}^{1+}$  precursors to yield bis- $\mu$ -oxo ( $\text{Cu}^{3+}$ )<sub>2</sub> dimers.<sup>15–17</sup> Typically, initial formation of a 1:1  $\text{Cu}/\text{O}_2$  adduct is followed by reaction with a second  $\text{Cu}^{1+}$  to form a  $\mu\text{-}\eta^2\text{:}\eta^2$  side-on peroxo bridged ( $\text{Cu}^{2+}$ )<sub>2</sub> intermediate that subsequently rearranges to a bis- $\mu$ -oxo ( $\text{Cu}^{3+}$ )<sub>2</sub> complex through reductive O–O bond cleavage.<sup>1</sup> Alternatively, only relatively few bis- $\mu$ -oxo ( $\text{Ni}^{3+}$ )<sub>2</sub> dimers have been reported so far, all of which possess nitrogen supporting ligands.<sup>5–7</sup> In the majority of these dimers the Ni atoms are 5-fold coordinated,<sup>5,7</sup> and the dimer adopts an anti conformation as shown in Chart 1. Unlike bis- $\mu$ -oxo ( $\text{Cu}^{3+}$ )<sub>2</sub> dimers, these ( $\text{Ni}^{3+}$ )<sub>2</sub> dimers cannot be obtained upon reaction of a  $\text{Ni}^{1+}$  precursor with  $\text{O}_2$ ; instead, the corresponding bis- $\mu$ -hydroxo ( $\text{Ni}^{2+}$ )<sub>2</sub> complexes must be reacted with  $\text{H}_2\text{O}_2$ . On the basis of kinetic studies it has been postulated that this reaction involves a  $\mu\text{-}\eta^2\text{:}\eta^2$  peroxo ( $\text{Ni}^{2+}$ )<sub>2</sub> intermediate.<sup>7</sup>

However, very recently we discovered that  $[(\text{PhTt}^{\text{Bu}})_2\text{Ni}^{1+}\text{CO}]$ , where  $(\text{PhTt}^{\text{Bu}})$  is a tridentate thioether ligand,<sup>18</sup> is capable

of activating  $\text{O}_2$ , yielding a species formulated as  $[(\text{PhTt}^{\text{Bu}})_2\text{Ni}_2(\mu\text{-O})_2]$  (**1**).<sup>19</sup> The molecular structure of **1** was determined on the basis of complementary low-temperature spectroscopic studies. XAS data of **1** are consistent with the  $\text{Ni}^{3+}$  oxidation state, and EXAFS studies corroborate the  $(\text{Ni}^{3+})_2(\mu\text{-O})_2$  core structure. EPR and  $^1\text{H}$  NMR data reveal that the dimer is diamagnetic at 77 K, indicating that the  $\text{Ni}^{3+}$  ions are antiferromagnetically exchange-coupled. The electronic absorption spectrum exhibits a prominent band at  $17\,700\text{ cm}^{-1}$  ( $\epsilon = 16\,000\text{ M}^{-1}\text{ cm}^{-1}$ ), which has been ascribed to an  $\text{O} \rightarrow \text{Ni}$  charge transfer (CT) transition.<sup>19</sup> As **1** is formed by  $\text{O}_2$  activation of a  $\text{Ni}^{1+}$  precursor, it is conceivable that this reaction follows a similar mechanism as established for the copper complexes involving stepwise formation of  $\text{Ni}/\text{O}_2$  and  $\mu\text{-}\eta^2\text{:}\eta^2$  peroxo ( $\text{Ni}^{2+}$ )<sub>2</sub> intermediates. However, while side-on peroxo and bis- $\mu$ -oxo  $\text{Cu}_2$  isomers can coexist in equilibrium depending on the nature of the supporting ligands employed,<sup>15,20–24</sup> experimental evidence for the formation of side-on peroxo ( $\text{Ni}^{2+}$ )<sub>2</sub> intermediates has yet to be provided.

Molecular-level understanding of the reactivity of Ni complexes toward  $\text{O}_2$  requires detailed knowledge of the  $\text{Ni}_2\text{O}_2$  core electronic structure in the corresponding bis- $\mu$ -oxo dimers. While several spectroscopic and theoretical studies performed by Solomon, Stack, and co-workers<sup>25</sup> and Tolman and co-workers<sup>2,26</sup> provided detailed insight into  $\text{Cu}-\text{O}$  bonding in bis- $\mu$ -oxo ( $\text{Cu}^{3+}$ )<sub>2</sub> dimers, the nature of  $\text{Ni}-\text{O}$  bonding in bis- $\mu$ -oxo ( $\text{Ni}^{3+}$ )<sub>2</sub> dimers remains largely unexplored. In this paper a detailed spectroscopic and computational study on the bis- $\mu$ -oxo ( $\text{Ni}^{3+}$ )<sub>2</sub> dimer **1** is presented. The  $\text{Ni}-\text{O}$  bond strength in **1**, determined from a normal coordinate analysis (NCA) of our resonance Raman (rR) data, is compared to that in ( $\text{Ni}^{3+}$ )<sub>2</sub> dimers with nitrogen supporting ligands and to the  $\text{Cu}-\text{O}$  bond strength in bis- $\mu$ -oxo ( $\text{Cu}^{3+}$ )<sub>2</sub> dimers. Absorption, circular dichroism (CD), and magnetic circular dichroism (MCD) spectroscopic techniques are used in conjunction with density functional theory (DFT) electronic structure calculations to generate an experimentally calibrated bonding description for **1**. To explore the possible role of the thioether ligands in the formation and stabilization of **1**, computations are also presented on a representative example of a bis- $\mu$ -oxo ( $\text{Ni}^{3+}$ )<sub>2</sub> dimer possessing tridentate nitrogen supporting ligands (Chart 1).<sup>18</sup> To explore whether differences in  $\text{M}_2\text{O}_2$  core electronics relate to differences in the reactivities of  $\text{Ni}_2$  and  $\text{Cu}_2$  dimers, additional computations are described on a hypothetical  $[(\text{PhTt}^{\text{Bu}})_2\text{Ni}_2(\mu\text{-}\eta^2\text{:}\eta^2\text{-O}_2)]$  complex (**2**) corresponding to the putative side-on peroxo ( $\text{Ni}^{2+}$ )<sub>2</sub> intermediate in the formation of **1**, and the

- (5) (a) Hikichi, S.; Yoshizawa, M.; Sasakura, Y.; Akita, M.; Moro-oka, Y. *J. Am. Chem. Soc.* **1998**, *120*, 10567. (b) Hikichi, S.; Yoshizawa, M.; Sasakura, Y.; Komatsuzaki, H.; Moro-oka, Y.; Akita, M. *Chem.-Eur. J.* **2001**, *7*, 5012.
- (6) Shiren, K.; Ogo, S.; Fujinami, S.; Hayashi, H.; Suzuki, M.; Uehara, A.; Watanabe, Y.; Moro-oka, Y. *J. Am. Chem. Soc.* **2000**, *122*, 254.
- (7) Itoh, S.; Bandoh, H.; Nakagawa, M.; Nagamoto, S.; Kitagawa, T.; Karlin, K. D.; Fukuzumi, S. *J. Am. Chem. Soc.* **2001**, *123*, 11168.
- (8) (a) Solomon, E. I.; Tuzcek, F.; Root, D. E.; Brown, C. A. *Chem. Rev.* **1994**, *94*, 827. (b) Solomon, E. I.; Sundaram, U. M.; Machonkin, T. E. *Chem. Rev.* **1996**, *96*, 2563.
- (9) Sánchez-Ferrer, A.; Rodríguez-López, J. N.; García-Cánovas, F.; García-Carmona, F. *Biochim. Biophys. Acta* **1995**, *1247*, 1.
- (10) Krebs, B. In *Bioinorganic Chemistry: An Inorganic Perspective of Life*; Kessissoglou, D. P., Ed.; Kluwer Academic: Dordrecht, The Netherlands, 1995.
- (11) Waller, B. J.; Lipscomb, J. D. *Chem. Rev.* **1996**, *96*, 2625.
- (12) Solomon, E. I.; Brunold, T. C.; Davis, M. I.; Kemsley, J. N.; Lee, S.-K.; Lehnert, N.; Neese, F.; Skulan, A. J.; Yang, Y.-S.; Zhou, J. *Chem. Rev.* **2000**, *200*, 235–349.
- (13) Shu, L.; Nesheim, J. C.; Kauffmann, K.; Münck, E.; Lipscomb, J. D.; Que, L., Jr. *Science* **1997**, *275*, 515.
- (14) (a) Valentine, A. M.; Lippard, S. J. *Chem. Soc., Dalton Trans.* **1997**, 3925. (b) Kurtz, D. M., Jr. *J. Biol. Inorg. Chem.* **1997**, *2*, 159. (c) Riggs-Gelasco, P. J.; Shu, L.; Chen, S.; Burdi, D.; Huynh, B. H.; Que, L., Jr. *J. Am. Chem. Soc.* **1998**, *120*, 849. (d) Que, L., Jr.; Dong, Y. *Chem. Res.* **1996**, *29*, 190. (e) Que, L., Jr. *J. Chem. Soc., Dalton Trans.* **1997**, 3933.
- (15) Halfen, J. A.; Mahapatra, S.; Wilkinson, E. C.; Kaderli, S.; Young, V. G., Jr.; Que, L., Jr.; Zuberbühler, A. D.; Tolman, W. B. *Science* **1996**, *271*, 1397.
- (16) Mahapatra, S.; Kaderli, S.; Llobet, A.; Neuhold, Y.-M.; Palanché, T.; Halfen, J. A.; Young, V. G., Jr.; Kaden, T. A.; Que, L., Jr.; Zuberbühler, A. D.; Tolman, W. B. *Inorg. Chem.* **1997**, *36*, 6343.
- (17) Itoh, S.; Taki, M.; Nakao, H.; Holland, P. L.; Tolman, W. B.; Que, L., Jr.; Fukuzumi, S. *Angew. Chem.* **2000**, *112*, 409; *Angew. Chem., Int. Ed.* **2000**, *39*, 398.

- (18) Abbreviations:  $\text{PhTt}^{\text{Bu}}$ , phenyl-tris(*tert*-butylthio)methylborate;  $\text{Me}_2\text{Et}_2\text{chd}$ , *N,N'*-dimethyl-*N,N'*-diethylcyclohexyldiamine;  $\text{Tp}^{\text{Me}_3}$ , hydrotris(3,4,5-methyl-1-pyrazolyl)borate;  $^i\text{PrTACN}$ , 1,4,7-trisopropyl-1,4,7-triazacyclononane.
- (19) Mandimutsira, B. S.; Yamarik, J. L.; Brunold, T. C.; Gu, W.; Cramer, S. P.; Riordan, C. G. *J. Am. Chem. Soc.* **2001**, *123*, 9194.
- (20) Obias, H. V.; Lin, Y.; Murthy, N. N.; Pidcock, E.; Solomon, E. I.; Ralle, M.; Blackburn, N. J.; Neubold, Y. M.; Zuberbühler, A. D.; Karlin, K. D. *J. Am. Chem. Soc.* **1998**, *120*, 12960.
- (21) Pidcock, E.; DeBeer, S.; Obias, H. V.; Hedman, B.; Hodgson, K. O.; Karlin, K. D.; Solomon, E. I. *J. Am. Chem. Soc.* **1999**, *121*, 1870.
- (22) Cahoy, J.; Holland, P. L.; Tolman, W. B. *Inorg. Chem.* **1999**, *38*, 2161.
- (23) Hayashi, H.; Fujinami, S.; Nagamoto, S.; Ogo, S.; Suzuki, M.; Uehara, A.; Watanabe, Y.; Kitagawa, T. *J. Am. Chem. Soc.* **2000**, *122*, 2124.
- (24) Mahadevan, V.; Henson, M.; Solomon, E. I.; Stack, T. D. P. *J. Am. Chem. Soc.* **2000**, *122*, 10249.
- (25) Henson, M. J.; Mukherjee, P.; Root, D. E.; Stack, T. D. P.; Solomon, E. I. *J. Am. Chem. Soc.* **1999**, *121*, 10332.
- (26) Holland, P. L.; Cramer, C. J.; Wilkinson, E. C.; Mahapatra, S.; Rodgers, K. R.; Itoh, S.; Taki, M.; Fukuzumi, S.; Que, L., Jr.; Tolman, W. B. *J. Am. Chem. Soc.* **2000**, *122*, 792.

reaction coordinate for the conversion of the side-on peroxo species **2** to the bis- $\mu$ -oxo complex **1** is evaluated.

## 2. Experimental Section

**2.1. Spectroscopy.** Samples of  $[(\text{PhTi}^{\text{Bu}})_2\text{Ni}_2(\mu\text{-O})_2]$  **1** were obtained upon reaction of the  $\text{Ni}^{1+}$  precursor  $[(\text{PhTi}^{\text{Bu}})\text{NiCO}]$  with  $\text{O}_2$  as described in ref 19. Absorption, CD, and MCD spectra of a 0.5 mM solution of **1** in toluene were recorded at 190 K using a spectropolarimeter (Jasco J-715) with a sample compartment modified to accommodate a superconducting magnetocryostat (Oxford Instruments SM-4000). rR spectra of isotopically pure samples of **1** prepared with either  $^{16}\text{O}_2$  or  $^{18}\text{O}_2$  were recorded upon excitation with an  $\text{Ar}^+$  ion laser (Coherent I-305) or a dye laser (Coherent 599-01 equipped with rhodamine 6G dye) pumped by the  $\text{Ar}^+$  laser with incident laser power of 10–20 mW at the sample. Raman scattered light was collected at an  $\sim 135^\circ$  backscattering angle from the surface of a frozen solution of **1** contained in an NMR tube, which was immersed in a liquid  $\text{N}_2$ -filled EPR dewar. The scattered light was dispersed by a triple monochromator (Acton Research) using 1200 and 2400 grooves/mm gratings and detected by a back-illuminated CCD camera (Princeton Instruments,  $1340 \times 100$  pixels). Raman shifts and intensities were calibrated relative to the  $784\text{ cm}^{-1}$  peak of toluene.<sup>27</sup>

**2.2. Normal Coordinate Analysis.** A normal coordinate analysis (NCA) of the vibrational data was performed on the  $\text{Ni}_2\text{O}_2$  core structure with an idealized  $D_{2h}$  geometry using the interatomic distances  $\text{Ni}-\text{O} = 1.82\text{ \AA}$  and  $\text{Ni}\cdots\text{Ni} = 2.83\text{ \AA}$  derived from an EXAFS study.<sup>19</sup> The analysis was based on the Wilson FG matrix method using a Urey–Bradley force field as implemented in a modified version of the Schachtschneider program.<sup>28</sup>

**2.3. Electronic Structure Calculations.** DFT computations were performed on a home-built cluster composed of eight Pentium III processors using the Amsterdam density functional (ADF) 2000.02 software package.<sup>29</sup> Calculations on **1** were performed on a simplified molecular structure in which the phenyl and *tert*-butyl groups were substituted by methyl groups. The atomic coordinates of **1** were obtained through energy minimization by using the algorithm of Versluis and Ziegler<sup>30</sup> as implemented in ADF 2000.02. For single-point calculations on **3** the coordinates were taken from the crystal structure,<sup>5</sup> and the methyl groups were replaced by hydrogen atoms. The atomic coordinates for all models described in the text are included in the Supporting Information (Tables S1–S6). All calculations were carried out using an integration constant of 4.0, the Vosko–Wilk–Nusair local density approximation (VWN-LDA)<sup>31</sup> for the exchange and correlation energies, and the nonlocal gradient corrections of Becke<sup>32</sup> and Perdew.<sup>33</sup> A triple- $\zeta$  Slater-type orbital (STO) basis set with a single- $\zeta$  STO polarization function (ADF basis set IV) was used for all atoms. Core orbitals were frozen through 1s (C, N, and O) and 2p (S and Ni). Excited-state transition energies were calculated by the Slater transition state method.<sup>34</sup>

To allow for graphical output of key MOs and to obtain an independent assessment of the calculated bonding description for **1**,<sup>35</sup>

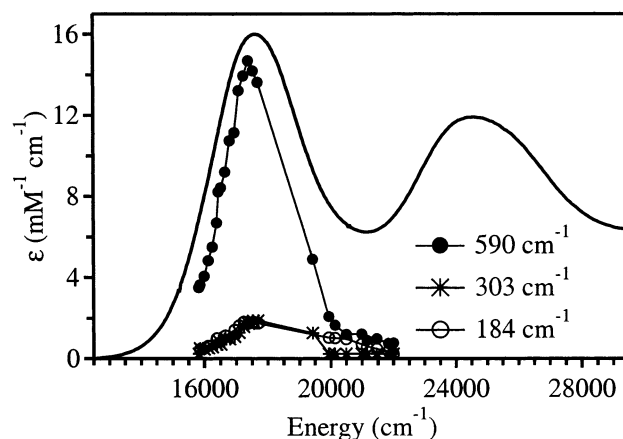


**Figure 1.** 210 K electronic absorption spectrum (solid line) of  $[(\text{PhTi}^{\text{Bu}})_2\text{Ni}_2(\mu\text{-O})_2]$  superimposed by rR excitation profiles (symbols) of the dominant vibrational features observed at 590, 303, and  $184\text{ cm}^{-1}$ .

additional single-point DFT calculations on **1** were performed using the electronic structure calculation package ORCA 2.1.80 developed by Dr. Frank Neese (MPI Mülheim, Germany).<sup>36</sup> A Perdew–Wang parametrization of LDA (PW-LDA)<sup>37</sup> with the nonlocal gradient corrections of Becke<sup>32</sup> and Perdew<sup>33</sup> was employed. For the Ni, O, and S atoms a triple- $\zeta$  Gaussian-type orbital (GTO) basis (Ahlrichs TZV)<sup>38</sup> was chosen with three, two, and one polarization functions, respectively.<sup>39,40</sup> The remaining atoms were modeled with the DGauss valence double- $\zeta$  basis<sup>41</sup> with one polarization function.<sup>39</sup> Isosurface plots (isodensity value  $0.03\text{ b}^{-3}$ ) of the MOs obtained from the ORCA calculations were generated using the GOpenMol software program developed by Leif Laaksonen.<sup>42</sup>

## 3. Results and Analysis

**3.1. Spectroscopy. A. Absorption and rR.** The electronic absorption spectrum of **1** at 210 K is dominated by two intense, broad bands centered at  $17\,700\text{ cm}^{-1}$  ( $\epsilon = 16\,000\text{ M}^{-1}\text{ cm}^{-1}$ ) and  $24\,800\text{ cm}^{-1}$  ( $\epsilon = 12\,000\text{ M}^{-1}\text{ cm}^{-1}$ ) as shown in Figure 1.<sup>19</sup> To identify the nature of the corresponding transitions, rR data were collected using various excitation wavelengths. rR spectra of **1** excited at 565 nm (Figure 2) are governed by an intense peak at  $590\text{ cm}^{-1}$  that shifts to  $560\text{ cm}^{-1}$  for samples prepared with  $^{18}\text{O}_2$ .<sup>43</sup> This feature has previously been assigned to the totally symmetric Ni–O stretching mode of the  $\text{Ni}_2\text{O}_2$  core in **1**.<sup>19</sup> The isotopic shift of  $30\text{ cm}^{-1}$  compares well with the value of  $28\text{ cm}^{-1}$  calculated for a diatomic Ni–O harmonic oscillator. In bis- $\mu$ -oxo ( $\text{Cu}^{3+}$ )<sub>2</sub> dimers the corresponding feature is typically observed in the  $600\text{--}632\text{ cm}^{-1}$  range.<sup>44</sup> The rR excitation profile of the  $590\text{ cm}^{-1}$  feature of **1** mirrors the

- (27) Varsányi, G. *Assignments for Vibrational Spectra of Seven-hundred Benzene Derivatives*; Wiley & Sons: New York, 1974; p 49.
- (28) (a) Schachtschneider, J. H. Technical Report No. 57-65, Shell Development Company, Emeryville, CA, 1966. (b) Fuhrer, H.; Kartha, V. B.; Kidd, K. G.; Krueger, P. J.; Mantsch, H. H. *Computer Programs for Infrared Spectroscopy*; Bulletin No. 15; National Research Council of Canada: Ottawa, 1976.
- (29) (a) Baerends, E. J.; Ellis, D. E.; Ros, P. *Chem. Phys.* **1973**, 2, 42. (b) te Velde, G.; Baerends, E. J. *Int. J. Comput. Phys.* **1992**, 99, 84.
- (30) Versluis, L.; Ziegler, T. J. *Chem. Phys.* **1988**, 88, 322.
- (31) Vosko, S. H.; Wilk, L.; Nusair, M. *Can. J. Phys.* **1980**, 58, 1200.
- (32) Becke, A. D. *J. Chem. Phys.* **1986**, 84, 4524.
- (33) Perdew, J. P. *Phys. Rev. B* **1986**, 33, 8822.
- (34) Slater, J. C. *The Calculation of Molecular Orbitals*; John Wiley & Sons: New York, 1979.
- (35) Nearly identical results were obtained using the ADF and ORCA software packages, thus justifying our approach to list MO energies and compositions obtained from ADF calculations and to show isosurface plots (Figures 6 and 7) generated from ORCA output.

- (36) Neese, F. Max Planck Institute for Radiation Chemistry, D-45470 Mülheim/Ruhr, Germany; neese@mpi-muelheim.mpg.de.
- (37) Perdew, J. P.; Wang, Y. *Phys. Rev. B* **1992**, 45, 13245.
- (38) Schäfer, A.; Horn, H.; Ahlrichs, R. *J. Chem. Phys.* **1992**, 97, 2571.
- (39) The Ahlrichs (2d, 2p, 2d2fg, and 3p2df) polarization functions were obtained from the TurboMole basis set library under ftp.chemie.uni-karlsruhe.de/pub/basen.
- (40) The Ahlrichs auxiliary basis sets were obtained from the TurboMole basis set library under ftp.chemie.uni-karlsruhe.de/pub/jbasen: (a) Eichkorn, K.; Treutler, O.; Ohm, H.; Haser, M.; Ahlrichs, R. *Chem. Phys. Lett.* **1995**, 240, 283. (b) Eichkorn, K.; Weigend, F.; Treutler, O.; Ahlrichs, R. *Theor. Chem. Acc.* **1997**, 97, 119.
- (41) Godbout, N.; Salahub, D. R.; Andzelm, J.; Wimmer, E. *Can. J. Chem.* **1992**, 70, 560.
- (42) (a) Laaksonen, L. *J. Mol. Graphics* **1992**, 10, 33. (b) Bergman, D. L.; Laaksonen, L.; Laaksonen, A. *J. Mol. Graphics Modell.* **1997**, 15, 301.
- (43) In ref 19 slightly different values of 585 and  $555\text{ cm}^{-1}$  were reported for **1**. The difference is due to the fact that while in ref 19 the Raman shifts were calibrated using the  $984\text{ cm}^{-1}$  line of  $\text{Na}_2\text{SO}_4$  as an external standard, in the present work the  $784\text{ cm}^{-1}$  peak of toluene has been used as an internal standard, giving more accurate results.
- (44) See ref 26 and references therein.



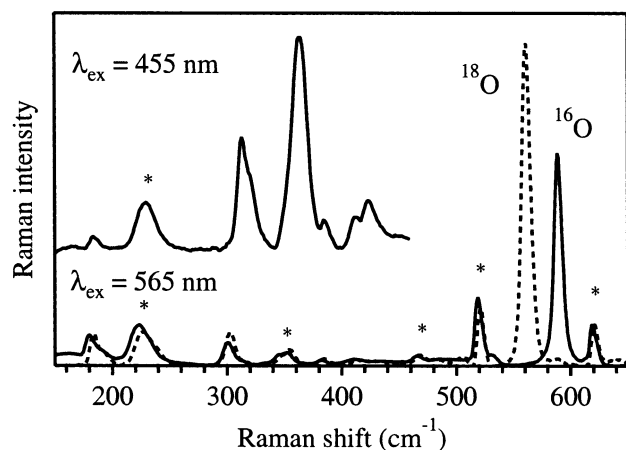


**Figure 2.** rR spectra of  $[(\text{PhT}^{\text{Bu}})_2\text{Ni}_2(\mu\text{-O})_2]$  at 77 K for 455 (top) and 565 nm (bottom) excitations. Solid and broken lines show spectra of  $^{16}\text{O}$  and  $^{18}\text{O}$  isotopically labeled samples, respectively. Solvent peaks are marked with an asterisk.

absorption band in the visible spectral region (Figure 1), indicating that the latter is due to an  $\text{O} \rightarrow \text{Ni}$  CT transition. Two additional, significantly weaker rR features are observed at 184 and  $303\text{ cm}^{-1}$ . Their enhancement behavior parallels that of the  $590\text{ cm}^{-1}$  peak (Figure 1); however, these features are not isotopically sensitive. In bis- $\mu$ -oxo ( $\text{Cu}^{3+}$ ) $_2$  dimers, the  $^{16}\text{O}/^{18}\text{O}$  insensitive symmetric  $\text{O}-\text{Cu}-\text{O}$  bending mode has been found in the  $118\text{--}133\text{ cm}^{-1}$  range.<sup>25</sup> Since the rR spectrum of **1** proved to be featureless below  $180\text{ cm}^{-1}$ , we tentatively assign the band at  $184\text{ cm}^{-1}$  to the  $\text{O}-\text{Ni}-\text{O}$  bending mode. Further support for this assignment will be provided in section 3.3.A. The band at  $303\text{ cm}^{-1}$  is clearly at too high a frequency for the  $\text{O}-\text{Ni}-\text{O}$  bending mode, but it is in the range expected for  $\text{Ni}-\text{S}$  stretching modes.<sup>45</sup> Enhancement of this feature for excitation in resonance with this  $\text{O} \rightarrow \text{Ni}$  CT transition can be explained in terms of coupling between  $\text{Ni}-\text{S}$  and  $\text{Ni}-\text{O}$  stretching modes (vide infra). Upon excitation at 455 nm, the rR spectrum of **1** exhibits additional, isotope-insensitive peaks at 313, 363, and  $415\text{ cm}^{-1}$  (Figure 2). These features are tentatively assigned to  $\text{Ni}-\text{S}$  stretches, suggesting that the absorption band at  $24\,800\text{ cm}^{-1}$  arises from a  $\text{S}$  (thioether)  $\rightarrow \text{Ni}$  CT transition.

To obtain further insight into the nature of the  $\text{O} \rightarrow \text{Ni}$  CT excited state at  $17\,700\text{ cm}^{-1}$ , the rR excitation profiles were analyzed in the framework of the time-dependent Heller theory.<sup>46</sup> Such an analysis yields dimensionless displacements  $\Delta_n$  of the excited state relative to the ground state along the relevant normal coordinates  $n$ , which will be used in section 3.4.B to estimate excited-state distortions. Because of the high quality of our rR data, the absolute magnitudes of the  $\Delta_n$  values could be obtained directly from fits of the calculated rR profiles to the experimental data. With values of  $|\Delta_{590}| = 2.1$ ,  $|\Delta_{184}| = 2.25$ , and  $|\Delta_{303}| = 1.35$ , the experimental rR profile data are very well reproduced (Figure 3).

**B. CD and MCD.** Figure 3 shows that the calculated absorption profile is significantly sharper than the experimental spectrum, suggesting that the band at  $17\,700\text{ cm}^{-1}$  is actually

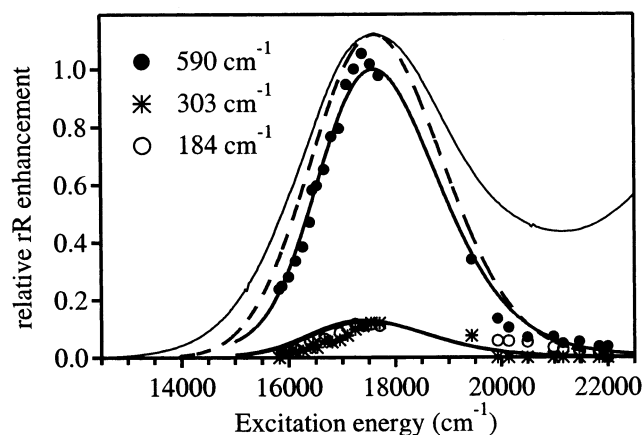


**Figure 3.** Simulated absorption spectrum (broken line) and rR excitation profile data (solid lines) using time-dependent Heller theory<sup>46</sup> with the dimensionless excited-state distortion parameters  $|\Delta_{184}| = 2.25$ ,  $|\Delta_{303}| = 1.35$ , and  $|\Delta_{590}| = 2.1$ . The experimental absorption spectrum (thin solid line) and rR excitation profile data (symbols) are shown for comparison.

composed of several overlapping components. To determine the number and intensities of the transitions contributing to this absorption band, CD and MCD spectra of **1** were measured at 190 and 230 K. The CD spectrum is completely featureless over the entire Vis and NIR range (not shown), consistent with a relatively symmetric  $\text{Ni}$ –ligand environment in **1**. In contrast, the 7 T, 190 K MCD spectrum of **1** exhibits three weak features between  $13\,000$  and  $23\,000\text{ cm}^{-1}$  (Figure 4). The intensity of these bands remains constant between 190 and 230 K, consistent with MCD B-term behavior. This result indicates that paramagnetic states are not significantly populated below 230 K, in line with the results from a  $^1\text{H}$  NMR study.<sup>19</sup> MCD data obtained above  $23\,000\text{ cm}^{-1}$  are affected by the presence of varying amounts of thermal decomposition products; thus, they are not considered further.

Simultaneous fits of MCD and absorption spectra below  $23\,000\text{ cm}^{-1}$  require a minimum of four Gaussians to achieve good agreement between simulated and experimental absorption spectra (see the dotted lines in Figure 4). A fifth band was included in our fit of the absorption spectrum to account for the band at  $24\,800\text{ cm}^{-1}$ . The fit parameters shown in Table 1 reveal that the  $17\,700\text{ cm}^{-1}$  absorption band is due predominantly to a single intense transition. Two additional transitions, labeled A and B, occur at  $15\,880$  and  $16\,070\text{ cm}^{-1}$ , respectively. Their almost equal intensities but opposite signs in the MCD spectrum are characteristic of a pseudo-A-term behavior involving two perpendicularly polarized transitions.<sup>47</sup> They are weak in absorption but relatively strong in the MCD spectrum, resulting in large  $\Delta\epsilon/\epsilon$  ratios (see Table 1) that permit their assignment as ligand-field transitions. Bands C and D form a second pair of equally intense but oppositely signed transitions in the MCD spectrum. The  $\Delta\epsilon/\epsilon$  ratio for band C is 2 orders of magnitude smaller than the ratios for bands A and B, which clearly reveals the CT character of the corresponding transition, consistent with our rR data (section 3.1.A). In summary, our MCD data of **1** reveal that four transitions occur between  $15\,880$  and  $20\,160\text{ cm}^{-1}$ ; however, a single transition is responsible for the intense absorption band centered at  $17\,700\text{ cm}^{-1}$ .

(45) Nakamoto, K. *Infrared and Raman Spectra of Inorganic and Coordination Compounds, Part B*, 5th ed.; John Wiley & Sons: New York, 1997.

(46) (a) Heller, E. J. *Acc. Chem. Res.* **1981**, *14*, 368. (b) Zink, J. I.; Kim Shin, K.-S. In *Advances in Photochemistry*; Volman, D. H., Hammond, G. S., Neckers, D. C., Eds.; John Wiley: New York, 1991; Vol. 16, p 119. (c) Heller, E. J. *J. Chem. Phys.* **1975**, *62*, 1544.

(47) Johnson, M. In *Physical Methods in Bioinorganic Chemistry*; Que, L., Jr., Ed.; University Science Books: Sausalito, CA, 2000; pp 233–285.

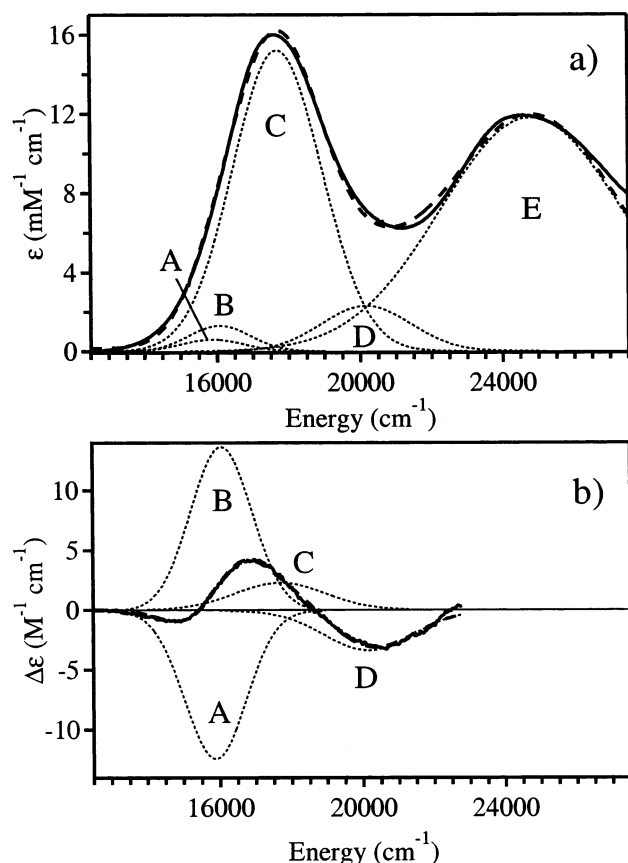


**Figure 4.** (a) 210 K absorption and (b) 190 K, 7 T MCD spectra of  $[(\text{PhTt}^{\text{Bu}})_2\text{Ni}_2(\mu\text{-O})_2]$  (solid lines). The dotted lines represent Gaussian band shape simulations for transitions A–E obtained using the fit parameters in Table 1. Their sums are shown by the dashed lines.

**Table 1.** Fit Parameters from Simultaneous Gaussian Resolutions of the Absorption and MCD Spectra of  $[(\text{PhTt}^{\text{Bu}})_2\text{Ni}_2(\mu\text{-O})_2]$  in Figure 3<sup>a</sup>

band	$\nu_{\text{max}}$	fwhm	$\epsilon$	$f$	$\Delta\epsilon$	$\epsilon/\Delta\epsilon$	assign. <sup>b</sup>
A	15 880	2 000	600	0.006	−12.4	0.0206	d→d
B	16 070	2 000	1 300	0.012	13.7	0.0105	d→d
C	17 700	2 950	15 200	0.205	2.3	0.0002	O→Ni CT
D	20 160	2 950	2 300	0.031	−3.3	0.0015	d→d
E	24 800	6 000	11 800	0.325	na <sup>c</sup>	na <sup>c</sup>	S→Ni CT

<sup>a</sup> Band maxima  $\nu_{\text{max}}$  and bandwidth at half-maximum (fwhm) are given in cm<sup>-1</sup>, and the molar extinction coefficients  $\epsilon$  and molar circular-dichroic extinction coefficients  $\Delta\epsilon$  are given in M<sup>-1</sup> cm<sup>-1</sup>. <sup>b</sup> Band assignments (see text for details). <sup>c</sup> Not available because of contributions from thermal decomposition products to the MCD spectrum in that region.

**3.2. Computations.** To complement our experimental data and to obtain quantitative insight into the electronic structure of  $[(\text{PhTt}^{\text{Bu}})_2\text{Ni}_2(\mu\text{-O})_2]$ , we performed both high-spin (HS) and broken-symmetry (BS,  $M_S = 0$ ) spin-unrestricted density functional calculations. The HS state with  $S = 1$ ,  $|M_S| = 1$  is the only pure spin state in an exchange-coupled dimer composed of two low-spin  $S = 1/2$   $\text{Ni}^{3+}$  centers that can be described by a single determinant. Alternatively, provided the two  $\text{Ni}^{3+}$  centers are high-spin  $S = 3/2$ , the only pure spin state that can be described by a single determinant is the HS state with  $S = 3$ ,  $|M_S| = 3$ . The BS wave functions, which contain contributions from all  $M_S = 0$  components of the exchange-coupled dimer ground state, are particularly useful for analysis of the super-exchange pathways because in the BS approach the dimer is

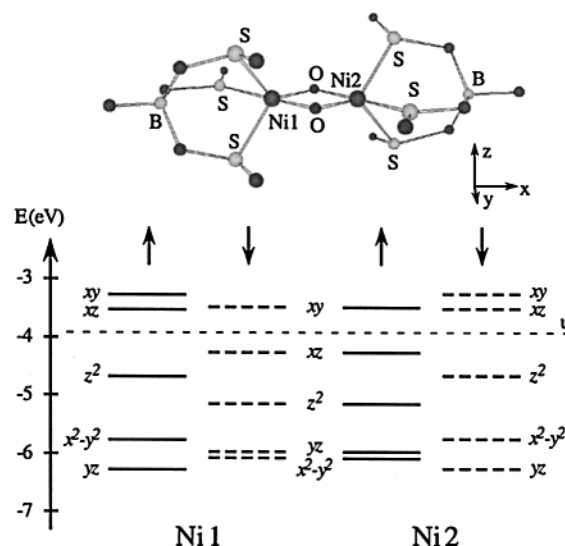


**Figure 5.** Energy level diagram obtained from a spin-unrestricted BS ( $M_S = 0$ ) DFT computation on the  $[(\text{PhTt}^{\text{Bu}})_2\text{Ni}_2(\mu\text{-O})_2]$  model. Spin-up and spin-down levels of the Ni d-based MOs are denoted by solid and broken lines, respectively. The computational model employed along with the molecular coordinate frame are shown on the top.

treated as two weakly interacting antiferromagnetically coupled monomers.<sup>48</sup>

Because no crystallographic data of **1** are available to date, the molecular structure was obtained by DFT geometry optimizations as described in section 2.3. Symmetry-unrestricted geometry optimizations were carried out for both the  $S = 1$  and the  $S = 3$  HS states associated with two ferromagnetically coupled low-spin ( $S = 1/2$ ) and high-spin ( $S = 3/2$ )  $\text{Ni}^{3+}$  centers, respectively, as well as for the corresponding BS ( $M_S = 0$ ) states (atomic coordinates are listed in Tables S1–S3). Table S7 compares the total energies and spin densities for the optimized dimer structures. The lowest energy was obtained for the BS state of the dimer composed of two low-spin  $\text{Ni}^{3+}$  centers, which is stabilized by  $-0.051$  eV relative to the corresponding HS ( $S = 1$ ) state. The HS ( $S = 3$ ) state of the dimer composed of two high-spin  $\text{Ni}^{3+}$  centers is 1.555 eV higher in energy than the HS ( $S = 1$ ) state of the dimer composed of two low-spin  $\text{Ni}^{3+}$  centers.<sup>49</sup> The calculation for the BS state of the dimer composed of two high-spin  $\text{Ni}^{3+}$  centers, starting with the optimized HS ( $S = 3$ ) geometry, was found to converge to the BS state composed of two low-spin  $\text{Ni}^{3+}$  centers,<sup>50</sup> indicating that the former state is at much higher energy than the latter. Together these results clearly indicate that **1** is best described as two antiferromagnetically coupled low-spin  $\text{Ni}^{3+}$  centers.

The molecular structure for the HS ( $S = 1$ ) state is shown in Figure 5.<sup>51</sup> The overall symmetry of the dimer complex is exactly  $C_2$  with the rotation axis perpendicular to the virtually planar  $\text{Ni}_2\text{O}_2$  core.<sup>52</sup> One sulfur atom of each ligand is situated

(48) Noodleman, L.; Norman, J. G., Jr. *J. Chem. Phys.* **1979**, *70*, 4903.

(49) In the HS ( $S = 3$ ) state, the Mulliken spin density on both oxo atoms is 0.92 (Table S7). These high values reflect the very covalent nature of the Ni–O bonds. The spin density of 1.45 on both  $\text{Ni}^{3+}$  centers is considerably lower than the expected value of 3, providing further evidence that the Ni–ligand environment in **1** does not support a high-spin electron configuration on  $\text{Ni}^{3+}$ .

(50) This calculation was found to converge to the BS state derived from two low-spin  $\text{Ni}^{3+}$  centers even with “Modify Start Potential 5/2”, a value typically used for high-spin  $\text{Fe}^{3+}$  centers.

(51) The structure obtained for the corresponding BS state is nearly identical; key interatomic distances read: Ni–O, 1.82/1.85 Å; Ni–S, 2.33 Å; Ni···Ni, 2.77 Å; and O···O, 2.41 Å.

trans to one of the Ni–O bonds and lies close to the plane defined by the  $\text{Ni}_2\text{O}_2$  core. The Ni–O bonds that are trans to these in-plane Ni–S bonds are slightly longer (1.86 Å) than their cis counterparts (1.81 Å). Overall these distances agree well with the value of 1.82 Å obtained from EXAFS experiments.<sup>19</sup> The Ni···Ni and O···O distances are 2.76 (EXAFS: 2.83 Å) and 2.42 Å, respectively. The average Ni–S distance is 2.35 Å, in very good agreement with the value of 2.34 Å derived from EXAFS data. The three S–Ni–S bonding angles at each Ni center vary only slightly between 88 and 92°, indicating an almost perfectly 3-fold symmetric binding mode of the thioether ligand. This result is consistent with <sup>1</sup>H NMR data,<sup>19</sup> which show a single resonance for the three *tert*-butyl groups. The good agreement between experimental and calculated bond distances and angles demonstrates that the dimer shown in Figure 5 provides a reasonable structural model for **1**. In contrast, in the geometry-optimized model possessing a HS  $S = 3$ ,  $|M_S| = 3$  ground state, corresponding to two ferromagnetically coupled high-spin  $\text{Ni}^{3+}$  centers, the average Ni–O and Ni–S bond lengths are increased to 1.90 and 2.43 Å, respectively, while the Ni···Ni distance decreased to 2.66 Å. These values are inconsistent with the EXAFS data for **1**,<sup>19</sup> corroborating our conclusion drawn above that the  $\text{Ni}^{3+}$  centers in **1** possess a low-spin electron configuration.

The overall dimer symmetry obtained from the symmetry-unconstrained geometry optimization (Figure 5) is very close to  $C_{2h}$ . Such a symmetric  $\text{Ni}_2\text{O}_2$  core is consistent with the absence of any detectable features in the CD spectrum of **1** (see section 3.1.B), which indicates that **1** probably possesses an inversion center, as would be the case in  $C_{2h}$  symmetry. Therefore, we performed an additional geometry optimization for the HS ( $S = 1$ ,  $|M_S| = 1$ ) state by imposing  $C_{2h}$  symmetry with  $\sigma_h$  lying in the *xy* plane (i.e., containing the  $\text{Ni}_2\text{O}_2$  core) (Figure 5). While the changes in optimized bond lengths and angles are negligible<sup>53</sup> (Table S4 lists the atomic coordinates), imposing  $C_{2h}$  dimer symmetry greatly facilitates analysis of the key bonding interactions and the MOs involved in the observed electronic transitions of **1** (sections 3.3 and 3.4).

**3.3. Ground-State Properties. A. Normal Coordinate Analysis.** To determine the Ni–O bond strength and to obtain the eigenvectors of the normal modes associated with the  $\text{Ni}_2\text{O}_2$  unit, a normal coordinate analysis (NCA) was performed on the rR data of **1**. The fact that (i) the totally symmetric Ni–O breathing mode produces by far the most intense feature in the rR spectrum of **1** upon excitation in resonance with the 17 700  $\text{cm}^{-1}$  feature, whereas contributions from Ni–S stretches are minor (Figure 2), and that (ii) the magnitude of the  $^{16}\text{O}_2 \rightarrow ^{18}\text{O}_2$  shift for this mode only slightly deviates from the value of an isolated Ni–O harmonic oscillator indicates that this mode is well-represented using only the four atoms of the  $\text{Ni}_2\text{O}_2$  core in the NCA. A Urey–Bradley force field originally developed for the description of the core vibrations in  $\mu\text{-}\eta^2\text{:}\eta^2$  peroxo ( $\text{Cu}^{2+}$ )<sub>2</sub> dimers<sup>54</sup> was adapted as follows: to limit the number of parameters a  $D_{2h}$   $\text{Ni}_2\text{O}_2$  core geometry was used, the out-of-plane mode was neglected, and the O–Ni–O and Ni–O–Ni bending modes were modeled with a single force constant  $k_\delta$ , which is justified by the fact that the two bending modes

**Table 2.** Experimental and Calculated Vibrational Frequencies for  $[(\text{PhT}^{\text{Bu}})_2\text{Ni}_2(\mu\text{-O})_2]^a$

normal mode	sym	exptl freqs		normal coordinate analysis		
		<sup>16</sup> O <sub>2</sub>	<sup>18</sup> O <sub>2</sub>	<sup>16</sup> O <sub>2</sub>	<sup>18</sup> O <sub>2</sub>	force constants
$\delta_s(\text{O–Ni–O})$	a <sub>g</sub>	184	184	185	183	$k_\delta = 0.20$ (0.05) <sup>b</sup>
$\delta_{as}(\text{Ni–O–Ni})$	b <sub>2u</sub>			551	526	
$\nu_s(\text{Ni–O})$	a <sub>g</sub>	590	560	587	561	$k_{\text{Ni–O}} = 2.64$
$\nu_{as}(\text{Ni–O})$	b <sub>1g</sub>			630	600	
$\delta_{as}(\text{O–Ni–O})$	b <sub>3u</sub>			666	637	

<sup>a</sup> Calculated values were obtained from a normal coordinate analysis (NCA) of the  $\text{Ni}_2\text{O}_2$  unit. Frequencies are given in  $\text{cm}^{-1}$ , and stretching and bending force constants  $k$  are given in  $\text{mdyn}/\text{\AA}$  and  $\text{mdyn}/\text{rad}^2$ , respectively. <sup>b</sup> Urey–Bradley nonbonding interaction constant in  $\text{mdyn}/\text{\AA}$ .

**Table 3.** Normal Mode Descriptions for the  $\text{Ni}_2(^{16}\text{O})_2$  Unit

normal mode	sym	eigenvectors <sup>a</sup>			PED <sup>b</sup>		
		Ni–O	O···O	O–Ni–O	Ni–O	O–Ni–O	UB <sup>c</sup>
$\delta_s(\text{O–Ni–O})$	a <sub>g</sub>	0.011	0.167	0.128	5.9	64.6	29.5
$\delta_{as}(\text{Ni–O–Ni})$	b <sub>2u</sub>	±0.125	0.000	0.000	92.9	6.5	0.5
$\nu_s(\text{Ni–O})$	a <sub>g</sub>	0.132	0.312	0.103	90.5	4.2	5.3
$\nu_{as}(\text{Ni–O})$	b <sub>1g</sub>	±0.149	0.000	0.000	100	0	0
$\delta_{as}(\text{O–Ni–O})$	b <sub>3u</sub>	±0.155	0.000	±0.138	96.8	2.9	0.2

<sup>a</sup> Mass-weighted eigenvectors  $L_n$ . <sup>b</sup> Potential energy distribution (PED) in %. <sup>c</sup> Urey–Bradley nonbonded interaction.

are fully correlated in a planar  $\text{Ni}_2\text{O}_2$  core. An initial estimate of  $k_{\text{Ni–O}} = 2.70$   $\text{mdyn}/\text{\AA}$  was used on the basis of the reported value for the bis- $\mu$ -oxo ( $\text{Cu}^{3+}$ )<sub>2</sub> dimer  $[(\text{Me}_2\text{Et}_2\text{chd})_2\text{Cu}_2(\mu\text{-O})_2]^{2+}$  (**3**), possessing a bidentate amine supporting ligand on each  $\text{Cu}^{3+}$  center.<sup>18,25</sup> The nonmodal force constant  $k_{\text{O–O}}$  was set to 0  $\text{mdyn}/\text{\AA}$ , and a value of  $k_{\text{UB}} = 0.05$   $\text{mdyn}/\text{\AA}$  was used for the Urey–Bradley nonbonding interaction that couples the Ni–O stretching and O–Ni–O bending modes. The force constants  $k_{\text{Ni–O}}$  and  $k_{\text{O–Ni–O}}$  were then fit to the experimental frequencies.

The calculated frequencies obtained with the fitted force constants agree well with the experimental values (Table 2), thus lending credence to the normal mode descriptions given in Table 3. The potential energy distribution (PED) contributions indicate that the totally symmetric  $\text{Ni}_2\text{O}_2$  breathing mode  $\nu_s(\text{Ni–O})$  involves predominantly Ni–O stretching motion. Therefore, doubling the value for  $k_{\text{UB}}$  to 0.10  $\text{mdyn}/\text{\AA}$  resulted in a change in  $k_{\text{Ni–O}}$  of less than 5%. In contrast,  $\delta(\text{O–Ni–O})$  depends strongly on the Urey–Bradley nonbonding interaction. Interestingly, using only the experimental  $\nu_s(\text{Ni–}^{16}\text{O}) = 590$   $\text{cm}^{-1}$  and  $\nu_s(\text{Ni–}^{18}\text{O}) = 560$   $\text{cm}^{-1}$  stretches in the fit,  $\delta_s(\text{O–Ni–O})$  is predicted at 176  $\text{cm}^{-1}$  ( $\Delta\nu(^{16}\text{O}_2/^{18}\text{O}_2) = 2.2$   $\text{cm}^{-1}$ ), thus supporting our assignment of the 184  $\text{cm}^{-1}$  rR feature to the symmetric O–Ni–O breathing mode (cf. section 3.1.A).

To facilitate a comparison of the force constants for the metal–oxo stretching modes in the bis- $\mu$ -oxo ( $\text{Ni}^{3+}$ )<sub>2</sub> and ( $\text{Cu}^{3+}$ )<sub>2</sub> dimers, we also performed a NCA on **3** using the same force field as described above along with the structural parameters and vibrational frequencies reported by Henson et al.<sup>25</sup> By systematically varying all other force constants within reasonable limits, a value of  $k_{\text{Cu–O}} = 2.82\text{--}2.90$   $\text{mdyn}/\text{\AA}$  was obtained for **3**. Thus,  $k_{\text{Cu–O}}$  is significantly higher than  $k_{\text{Ni–O}} = 2.64$   $\text{mdyn}/\text{\AA}$  for **1**. The electronic origin of this difference will be discussed in section 4.2.

**B. Nature of the Ni–O Bonds.** A major objective of this study is to explore the nature of the Ni–O bonds in **1**. Therefore,

(52) The rms out-of-plane deviation is 0.003 Å.

(53) Ni–O, 1.82/1.83 Å; Ni–S, 2.35 Å; Ni···Ni, 2.77 Å; and O···O, 2.38 Å.

(54) Baldwin, M. J.; Root, D. E.; Pate, J. E.; Fujisawa, K.; Kitajima, N.; Solomon, E. I. *J. Am. Chem. Soc.* **1992**, *114*, 10421.



**Table 4.** Energies (in eV) and Compositions (in %) of the Relevant Ni1 d-Based Molecular Orbitals Obtained from a BS DFT Calculation on the [(PhTt<sup>Bu</sup>)<sub>2</sub>Ni<sub>2</sub>(μ-O)<sub>2</sub>] Model<sup>a</sup>

level <sup>b</sup>	energy	left			bis-μ-oxo			right		
		S <sub>op</sub>	S <sub>ip</sub>	Ni1	p <sub>x</sub>	p <sub>y</sub>	p <sub>z</sub>	Ni2	S <sub>ip</sub>	S <sub>op</sub>
Unoccupied										
Ni1(xy),α	−3.223	8	6	42	20	9	0	3	0	0
Ni1(xy),β	−3.491	5	4	38	8	32	0	3	0	0
Ni1(xz),α	−3.511	25	0	42	0	0	18	3	0	0
Occupied										
Ni1(xz),β	−4.241	31	3	23	0	0	16	10	3	0

<sup>a</sup> Only Ni 3d, O 2p, and S 3p orbital contributions are shown. Contributions from C, H, and B atoms are negligible for these MOs. Electron density on the S atoms (denoted S<sub>op</sub> and S<sub>ip</sub> for out-of-plane and in-plane, respectively) is almost exclusively located in the p<sub>z</sub> orbitals. <sup>b</sup> α and β denote spin-up and spin-down MOs, respectively.

we also performed a spin-unrestricted BS ( $M_S = 0$ ) DFT calculation on **1** using the geometry-optimized  $C_{2h}$  model.<sup>55</sup> In the BS approach,<sup>48</sup> the symmetry elements connecting the two monomer halves of the dimer are removed, which allows the spin-up and spin-down electrons to localize on opposite sides of the dimer (see Figure 5). Table 4 lists the energies and compositions of the four relevant Ni1 d-based MOs obtained from a BS calculation on **1** with α and β denoting spin-up and spin-down MOs, respectively. The single unpaired electron on each Ni center occupies the xz-derived MO corresponding to Ni1(xz),β in Table 4.<sup>56,57</sup> As a consequence, this MO is strongly stabilized by −0.730 eV relative to its unoccupied minority-spin counterpart Ni1(xz),α because of spin polarization. This polarization effect also leads to a small stabilization of the other majority-spin MOs relative to their minority-spin analogues. The 10 Ni d-based MOs are in close energetic proximity to the highest-energy occupied ligand-based orbitals that carry significant thioether sulfur p<sub>z</sub> character. This small energy difference between metal and ligand orbitals, which reflects the high effective nuclear charge of Ni<sup>3+</sup>, results in significant mixing of Ni d orbitals with oxo and sulfur p orbitals (see Table 4).

The Ni–O bonding interactions can be inferred best from the Ni d-based unoccupied MOs that are antibonding with respect to the oxo ligand orbitals. Isosurface plots of these MOs localized on Ni1 are shown in Figure 6. The dominant Ni–O bonding interactions involve the Ni1(xy),α and Ni1(xy),β MOs, which are σ antibonding, and the Ni1(xz),α MO, which is π antibonding with respect to the Ni–O bond. These MOs have substantial contributions from the oxo p<sub>x</sub>, p<sub>y</sub> (Ni1(xy),α and Ni1(xy),β), and p<sub>z</sub> (Ni1(xz),α) atomic orbitals (Table 4), reflecting highly covalent Ni–O σ and π bonds, respectively. Since these MOs are unoccupied, their oxo p orbital character reflects the extent of O→Ni electron delocalization in the occupied MOs that stabilizes the high formal 3+ oxidation state of the Ni centers.

**C. Exchange Coupling.** The results of both <sup>1</sup>H NMR<sup>19</sup> and MCD spectroscopic studies indicate that the two Ni<sup>3+</sup> centers in **1** are antiferromagnetically coupled with an exchange parameter value of  $|J| \gtrsim 250 \text{ cm}^{-1}$  using the Heisenberg–

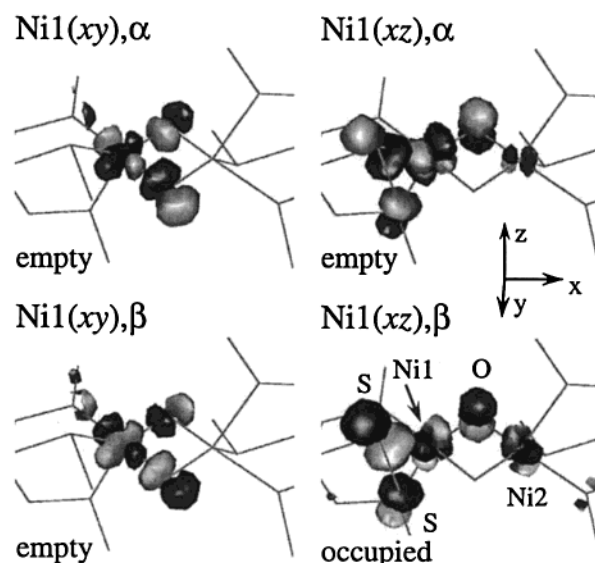


**Figure 6.** Isosurface plots (isodensity value 0.03 b<sup>−3</sup>) of the Ni1 d-based lowest unoccupied (xy(α), xy(β), and xz(α)) and highest occupied (xz(β)) MOs obtained from a BS ( $M_S = 0$ ) DFT calculation on the [(PhTt<sup>Bu</sup>)<sub>2</sub>Ni<sub>2</sub>(μ-O)<sub>2</sub>] model.

Dirac–Van Vleck Hamiltonian  $\mathcal{H} = -2J(\hat{S}_1 \cdot \hat{S}_2)$ . By employing the formalism developed by Noodleman,<sup>58</sup>  $J$  can be calculated from the total energies of the HS and BS states as follows:

$$J = (E_{\text{BS}} - E_{\text{HS}})/S_{\text{max}}^2 \quad (1)$$

With  $S_{\text{max}}^2 = 1$ , we obtain values of  $J = -347$  and  $-208 \text{ cm}^{-1}$  for the symmetry-unrestricted and  $C_{2h}$  geometry-optimized models of **1**, respectively. Our calculations thus reproduce the experimentally observed strong antiferromagnetic exchange interaction in **1**. The effectiveness of the Ni d-based MOs in mediating antiferromagnetic exchange interactions is governed by the extent of orbital contributions from the bridging oxides and the second nickel. Antiferromagnetic contributions to  $J$  arise from delocalization of unpaired electron spin density localized on Ni1 onto the half-filled Ni2-centered d orbitals and vice versa. Thus, the MO compositions in Table 4 reveal that the dominant superexchange pathway involves the Ni2(xz),α and Ni1(xz),β MOs that are π antibonding with respect to the oxo p<sub>z</sub> orbitals (Figure 6).

**3.4. Excited States. A. Spectral Assignments.** On the basis of our spectral analysis presented in section 3.1.B, five transitions labeled A–E are observed in the visible spectral range (Figure 4 and Table 1). Bands A, B, and D are readily assigned to ligand-field transitions because of their low absorption intensities and large  $\Delta\epsilon/\epsilon$  ratios (Table 1). In contrast, bands C and E possess high absorption intensities and small  $\Delta\epsilon/\epsilon$  ratios indicating their charge-transfer character. The Raman profile for the Ni–O stretching mode (Figure 1b) indicates that band C, centered at  $17\,700 \text{ cm}^{-1}$ , is associated with an O→Ni CT transition. Significantly, this transition is red-shifted by about  $8000 \text{ cm}^{-1}$  as compared to the lowest-energy O→Cu CT transition in bis-μ-oxo (Cu<sup>3+</sup>)<sub>2</sub> dimers.<sup>25</sup> To explore the origin

(55) Single-point BS calculations were performed on the geometry-optimized models of **1** obtained for both the HS ( $S = 1$ ) and the BS ( $M_S = 0$ ) dimer spin ground states. As the differences were insignificant, we report here the results of the single-point calculation on the HS geometry, as this calculation yields exact mirror images of the MOs localized on the two halves of the molecule.

(56) Throughout the manuscript, Ni d orbitals are labeled using an abbreviated notation (e.g., xy stands for d<sub>xy</sub>).

(57) As for the local coordinate system chosen the Ni xz and yz orbitals are strongly mixed in **1**, the designations Ni1(xz),α; Ni1(xz),β; Ni1(yz),α; Ni1(yz),β; Ni2(xz),α; Ni2(xz),β; Ni2(yz),α; and Ni2(yz),β are used solely for labeling purposes.

(58) Noodleman, L. *J. Chem. Phys.* **1981**, *74*, 5737.



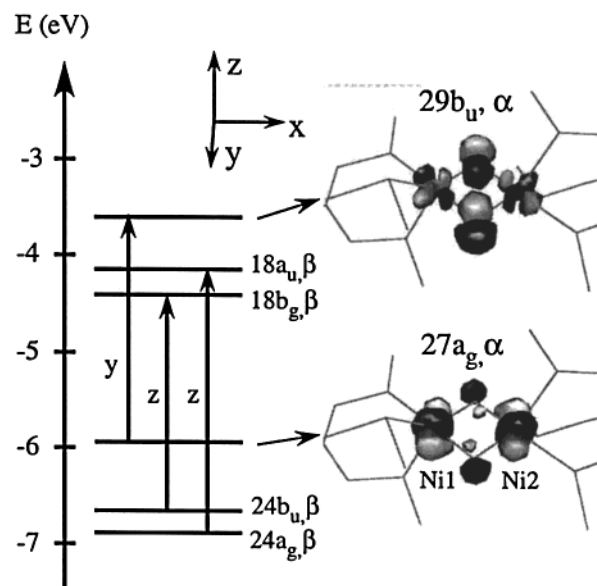
**Table 5.** Energies (in eV) and Compositions (in %) of the Ni d-Based and Relevant Ligand-Based Spin-Up Molecular Orbitals Obtained from a HS ( $S = 1$ ,  $|M_S| = 1$ ) DFT Calculation on the  $[(\text{PhTt}^{\text{Bu}})_2\text{Ni}_2(\mu\text{-O})_2]$  Model<sup>a</sup>

		Ni						bis- $\mu$ -oxo			S
level	MO <sup>b</sup>	energy	$x^2-y^2$	xy	xz	yz	$z^2$	$p_x$	$p_y$	$p_z$	tot
Unoccupied											
29a <sub>g</sub>	xy(+)	-3.475	0	38	0	0	3	29	0	0	21
29b <sub>u</sub>	xy(-)	-3.596	0	41	0	0	0	0	44	0	8
Occupied											
18a <sub>u</sub>	xz(+)	-4.146	0	0	23	4	0	0	0	18	40
18b <sub>g</sub>	yz(-)	-4.397	0	0	3	26	0	0	0	10	45
28b <sub>u</sub>	$z^2(-)$	-4.869	8	0	0	0	49	18	4	0	7
28a <sub>g</sub>	$z^2(+)$	-5.266	13	0	0	0	44	0	17	0	3
27a <sub>g</sub>	$x^2-y^2(+)$	-5.915	35	0	0	0	10	0	13	0	14
26b <sub>u</sub>	$x^2-y^2(-)$	-6.166	43	0	0	0	4	7	6	0	6
15b <sub>g</sub>	xz(-)	-6.256	0	0	56	0	0	0	0	0	19
15a <sub>u</sub>	yz(+)	-6.526	4	0	0	51	0	0	0	0	7
24b <sub>u</sub>	S <sub>op</sub> , p <sub>z</sub>	-6.663	0	0	0	0	0	0	6	0	26
24a <sub>g</sub>	S <sub>op</sub> , p <sub>z</sub>	-6.892	0	0	0	0	0	0	0	0	46

<sup>a</sup> Only Ni 3d, O 2p, and S 3p orbital contributions are shown. Contributions from C, H, and B atoms are negligible for these MOs. <sup>b</sup> MOs are labeled according to the atomic orbitals that produce the dominant contribution (i.e., either Ni 3d or out-of-plane  $S_{\text{op}}$  3p orbitals). The transformation behavior of each MO with respect to the  $C_2$  axis is indicated by “+” (symmetric) and “-” (antisymmetric).

of this marked bandshift, a detailed knowledge of the nature of the MOs involved in the O→Ni CT transition in **1** is necessary.

An important aspect of singly excited states in dimers is the fact that the locally excited configurations are not eigenfunctions of the dimer Hamiltonian. Instead, proper wave functions are obtained by taking the symmetric and antisymmetric combinations of these configurations. In contrast to the BS wave functions, the HS wave functions have proper dimer symmetry and are therefore better suited for analysis of the MOs involved in the key CT transitions of **1**.<sup>59</sup> Energies and compositions of the 10 Ni d-based spin-up MOs obtained from a spin-unrestricted HS calculation are listed in Table 5. These MOs arise from symmetric (+) and antisymmetric (-) combinations of the five monomeric Ni d orbitals with respect to the molecular  $C_2$  axis. The intensity of CT transitions can be related to the sum of overlaps of individual ligand orbital contributions to the corresponding donor and acceptor MOs.<sup>60</sup> Therefore, the MO compositions obtained from our HS computation greatly assist in assigning the absorption bands of **1** (Figure 4). From Table 5 three of the Ni d-based occupied spin-up MOs are found to have substantial oxo p character (i.e., levels 27a<sub>g</sub>, 28a<sub>g</sub>, and 28b<sub>u</sub>). The symmetric combination of the Ni  $x^2-y^2$  orbital (level 27a<sub>g</sub>) has a strong  $\sigma$  bonding interaction with the oxo  $p_y$  orbitals (Figure 7, bottom right). From level 27a<sub>g</sub>, only the transition to level 29b<sub>u</sub> is allowed in  $C_{2h}$  symmetry (i.e.,  $x^2-y^2(+)\rightarrow xy(-)$ ). As both the donor and the acceptor MOs have large contributions from the oxo  $p_y$  orbitals (Figure 7), this transition (which formally corresponds to a ligand-field transition based on the calculated MO descriptions but in fact carries significant O→Ni CT character due to electronic relaxation effects in the corresponding excited state) is expected to carry significant intensity in absorption. As MOs 27a<sub>g</sub> and 29b<sub>u</sub> are Ni–O  $\sigma$  bonding and  $\sigma$  antibonding, respectively, the Ni–O bonds are expected to weaken considerably upon 27a<sub>g</sub>→29b<sub>u</sub> excitation, consistent with

**Figure 7.** Energy level diagram showing the donor and acceptor MOs for the y polarized O→Ni and z polarized S→Ni CT transitions obtained from a spin-unrestricted HS ( $S = 1$ ,  $|M_S| = 1$ ) calculation on the  $[(\text{PhTt}^{\text{Bu}})_2\text{Ni}_2(\mu\text{-O})_2]$  model (left). Isosurface plots (isodensity value  $0.03 \text{ b}^{-3}$ ) of the donor and acceptor MOs for the dominant O→Ni CT transition at  $17\,700 \text{ cm}^{-1}$  (band C, Figure 4) are shown on the right.**Table 6.** Comparison of Experimental and Calculated Transition Energies (in  $\text{cm}^{-1}$ )

band <sup>a</sup>	transition <sup>b</sup>	pol <sup>c</sup>	obs	calcd
A	$z^2(-)$ , 28b <sub>u</sub> →xy(+), 29a <sub>g</sub>	x	15 880	11 265
B	$z^2(+)$ , 28a <sub>g</sub> →xy(-), 29b <sub>u</sub>	y	16 070	13 300
C	$x^2-y^2(+)$ , 27a <sub>g</sub> →xy(-), 29b <sub>u</sub>	y	17 700	18 000
D	$x^2-y^2(-)$ , 26b <sub>u</sub> →xy(+), 29a <sub>g</sub>	x	20 160	20 760
E	$S p_z$ , 24b <sub>u</sub> →yz(-), 18b <sub>g</sub>	z	24 800	26 370
	$S p_z$ , 24a <sub>g</sub> →xz(+), 18a <sub>u</sub>	z		29 270

<sup>a</sup> Band designations relate to Figure 3 and Table 1. <sup>b</sup> See Table 5 for MO compositions. <sup>c</sup> Band polarizations relate to the coordinate system in Figure 5.

our rR data for excitation in resonance with band C (section 3.4.B). Hence, band C is assigned to the 27a<sub>g</sub>→29b<sub>u</sub> (O→Ni) CT transition.

Antibonding interactions between the symmetric and the antisymmetric combinations of the Ni  $z^2$  orbitals and the oxo  $p_y$  and  $p_x$  orbitals in the 28a<sub>g</sub> and 28b<sub>u</sub> MOs, respectively, are small since the lobes of the Ni  $z^2$  orbitals are oriented perpendicular to the oxo  $p_x$  and  $p_y$  orbitals. Thus, these MOs have primarily Ni d orbital character, and the symmetry-allowed transitions originating from these levels, 28b<sub>u</sub>→29a<sub>g</sub> and 28a<sub>g</sub>→29b<sub>u</sub>, formally correspond to ligand-field transitions; they are therefore weak in absorption. As these transitions are calculated at lower energy than the 27a<sub>g</sub>→29b<sub>u</sub> transition corresponding to band C (Table 6), we tentatively assign bands A and B to the 28b<sub>u</sub>→29a<sub>g</sub> and 28a<sub>g</sub>→29b<sub>u</sub> transitions, respectively. On the basis of similar considerations, the weak absorption band D is assigned to the 26b<sub>u</sub>→29a<sub>g</sub> transition.

Further support for the above assignment comes from the MCD spectra in Figure 3. MCD intensity requires the presence of two perpendicular transition moments.<sup>47</sup> In complexes such as **1** that possess low symmetry and thus no orbitally degenerate states, this can be achieved through spin–orbit coupling among two excited states. In this case, the sum of the MCD intensities over two spin–orbit coupled excited states vanishes, which leads

(59) Note that the HS state is not actually populated at 200 K.

(60) (a) Ros, P.; Schuit, G. C. A. *Theor. Chim. Acta (Berlin)* **1966**, *4*, 1. (b) Van der Avoird, A.; Ros, P. *Theor. Chim. Acta (Berlin)* **1966**, *4*, 13.

**Table 7.** Comparison of the Ni<sub>2</sub>O<sub>2</sub> Core Interatomic Distances (in Å) in the Ground State and the 27a<sub>g</sub>→29b<sub>u</sub> (O→Ni) CT Excited State Corresponding to Band C of [(PhTt<sup>Et</sup>)<sub>2</sub>Ni<sub>2</sub>(μ-O)<sub>2</sub>]

bond vector	experimental <sup>a</sup>			calculated <sup>b</sup>		
	r(GS)	r(ES)	Δr	r(GS)	r(ES)	Δr
Ni–O <sub>cis</sub>	1.82	1.87	+0.05	1.82	1.84	+0.02
Ni–O <sub>trans</sub>	1.82	1.87	+0.05	1.83	1.90	+0.07
Ni···Ni	2.83	2.92	+0.09	2.77	2.93	+0.16
O···O	2.29	2.29	–0.005	2.38	2.33	–0.05
Ni–S <sup>c</sup>	2.34	na	na	2.35	2.35	0.00

<sup>a</sup> Experimental values are derived from EXAFS data (ground state, GS) and rR data in conjunction with a normal coordinate analysis (excited state, ES). <sup>b</sup> Calculated values are obtained from DFT geometry optimizations in the HS (*S* = 1, |*M<sub>S</sub>*| = 1) states. O<sub>cis</sub> and O<sub>trans</sub> denote the oxygen atoms oriented cis and trans to the in-plane Ni–S bonds. <sup>c</sup> Average value.

to characteristic derivative-shaped pseudo-A-term features. Bands A/B and C/D form two pairs of MCD pseudo-A-terms (see Figure 4). In the approximate *C*<sub>2h</sub> symmetry, all four transitions 27a<sub>g</sub>→29b<sub>u</sub>, 28a<sub>g</sub>→29b<sub>u</sub>, 28b<sub>u</sub>→29a<sub>g</sub>, and 26b<sub>u</sub>→29a<sub>g</sub> are allowed in either *x* or *y* polarization. The actual polarization of a transition is given by the direction of the electric dipole moment generated upon excitation. Both the 27a<sub>g</sub>→29b<sub>u</sub> and the 28a<sub>g</sub>→29b<sub>u</sub> transitions involve MOs that have substantial oxo p<sub>y</sub> character. The oxo p<sub>y</sub> orbitals in the donor and acceptor MOs are formally σ bonding and antibonding, respectively, with respect to the O···O vector. This results in a transition dipole moment oriented along the *y* axis. In contrast, the 28b<sub>u</sub>→29a<sub>g</sub> and 26b<sub>u</sub>→29a<sub>g</sub> transitions involve MOs with significant contributions from the oxo p<sub>x</sub> orbitals such that these transitions will have a nonzero transition dipole moment oriented along the *x* axis. Thus, the transition moments of the *y* polarized 27a<sub>g</sub>→29b<sub>u</sub> and *x* polarized 28a<sub>g</sub>→29b<sub>u</sub> transitions are mutually perpendicular, consistent with our assignment of the pseudo-A-term MCD feature composed of bands A and B to these transitions. By analogy, the *y* and *x* polarized transitions 28b<sub>u</sub>→29a<sub>g</sub> and 26b<sub>u</sub>→29a<sub>g</sub>, respectively, are responsible for the second pseudo-A-term composed of bands C and D.

Assignment of the intense absorption band E (Figure 4) that has been attributed to a S (thioether)→Ni CT transition on the basis of rR data (section 3.1.A) is complicated by the fact that several MOs have substantial contributions from thioether sulfur orbitals (Table 5). However, only transitions from the out-of-plane sulfur atoms are expected to be very strong because of the σ bonding interactions of the out-of-plane sulfur p<sub>z</sub> and Ni *xz*, *yz* orbitals.<sup>61</sup> Table 5 reveals that two potential donor MOs, 24a<sub>g</sub> and 24b<sub>u</sub>, have especially high contributions from out-of-plane sulfur p<sub>z</sub> orbitals. Transitions along the out-of-plane S–Ni vectors have to be *z* polarized. Therefore, the only two transitions that are allowed in *C*<sub>2h</sub> symmetry are 24a<sub>g</sub>→18a<sub>u</sub> and 24b<sub>u</sub>→18b<sub>g</sub>.<sup>62</sup> As the 18a<sub>u</sub> and 18b<sub>g</sub> acceptor MOs have large admixtures of out-of-plane sulfur p<sub>z</sub> orbitals, the 24a<sub>g</sub>→18a<sub>u</sub> and 24b<sub>u</sub>→18b<sub>g</sub> transitions have substantial out-of-plane sulfur p<sub>z</sub>→Ni *xz*, *yz* CT character and will give rise to intense absorption features. Both the 24a<sub>g</sub>→18a<sub>u</sub> and the 24b<sub>u</sub>→18b<sub>g</sub> S (thioether)→Ni CT transitions may thus contribute to the broad absorption feature centered at 24 800 cm<sup>–1</sup>.<sup>63</sup> The assignments

- (61) The in-plane sulfur p<sub>x</sub> and p<sub>y</sub> orbitals are involved in σ bonding interactions with Ni d orbitals and are therefore strongly stabilized such that corresponding excitations lie outside the experimentally accessible range.  
 (62) Although the 18a<sub>u</sub> and 18b<sub>g</sub> spin-up MOs are occupied, their spin-down counterparts are empty in the HS state and therefore can serve as acceptor MOs. The orbital compositions of the spin-up and spin-down MOs are very similar.

of bands A–E are summarized in Table 6. The DFT calculated energies agree favorably with the experimental values (Table 6), thus lending further support to the above band assignments.

**B. Excited-State Distortions.** To further our analysis of the O→Ni CT transition corresponding to band C (Figure 4), we performed an excited-state distortion analysis. Excited-state distortions can be expressed in terms of changes in internal coordinates using the eigenvectors obtained from the NCA (see Table 3) and the dimensionless displacements |Δ<sub>590</sub>| = 2.1 and |Δ<sub>184</sub>| = 2.25 from the quantitative rR analysis (section 3.1.A). The changes in internal coordinates Δ*r<sub>i</sub>* (Å) are related to displacements Δ<sub>*n*</sub> along normal coordinates by<sup>64</sup>

$$\Delta r_i = 5.8065 \sum_n L_{i,n} \frac{\Delta_n}{\sqrt{\nu_n}} \quad (2)$$

where *L<sub>i,n</sub>* is the *i*th element of the mass-weighted eigenvector *L<sub>n</sub>* for the *n*th normal mode. The nuclear distortions of the Ni<sub>2</sub>O<sub>2</sub> core upon O→Ni CT excitation using Δ<sub>590</sub> = +2.1 and Δ<sub>184</sub> = –2.25 are listed in Table 7. Since the signs of the displacements Δ are ambiguous, there are three other phase combinations of the distortions along ν(Ni–O) and the nonmodal ν(O···O) motions in addition to the one shown in Table 7. However, as the Ni–O bonds substantially weaken upon O→Ni CT excitation, they are expected to elongate, which indicates that Δ<sub>590</sub> > 0. Our choice of Δ<sub>184</sub> < 0 is based on a comparison with computational data obtained from optimization of the geometry of **1** in both the ground state and the O→Ni CT excited state (Table 7, right). Overall the computed and experimentally determined excited-state distortions agree well, thus lending credence to our choice of phase combinations. While the experimental value of +0.05 Å for the Ni–O distortion reflects an averaged value based on our NCA that assumes *D*<sub>2h</sub> symmetry, the computations predict that the trans Ni–O bonds undergo a significantly larger elongation (+0.07 Å) than the cis Ni–O bonds (+0.02 Å), the average change of +0.045 Å being in good agreement with the experimental value (+0.05 Å). We ascribe this asymmetry to a trans influence of the in-plane thioether S ligand atoms.

#### 4. Discussion

In recent years bis-μ-oxo (Ni<sup>3+</sup>)<sub>2</sub> dimers have become the focus of intense research in the fields of inorganic chemistry and catalysis.<sup>5–7,19</sup> However, very little is known to date about the nature of Ni–O bonding in these dimers, although knowledge of the electronic structure of the Ni<sub>2</sub>O<sub>2</sub> core is essential for tuning the reactivities of these complexes toward oxidative C–H abstraction, as has been described for several bis-μ-oxo (Ni<sup>3+</sup>)<sub>2</sub> dimers possessing chelating nitrogen supporting ligands. Previous spectroscopic<sup>2,25,26</sup> and theoretical<sup>65–68</sup> studies on the closely related bis-μ-oxo (Cu<sup>3+</sup>)<sub>2</sub> dimers provided a detailed

- (63) The bandwidth of band E in absorption is twice as large as that of band C, suggesting that band E is actually composed of multiple components.  
 (64) Myers, A. B.; Mathies, R. A. In *Biological Applications of Raman Spectroscopy*; Spiro, T. G., Ed.; Wiley: New York, 1987; Vol. 2, pp 1–58.  
 (65) Cramer, C. J.; Smith, B. A.; Tolman, W. B. *J. Am. Chem. Soc.* **1996**, *118*, 11283.  
 (66) Bérces, A. *Inorg. Chem.* **1997**, *36*, 4831.  
 (67) Liu, X.-Y.; Palacios, A. A.; Novoa, J. J.; Alvarez, S. *Inorg. Chem.* **1998**, *37*, 1202.  
 (68) Lam, B. M. T.; Halfen, J. A.; Young, V. G., Jr.; Hagadorn, J. R.; Holland, P. L.; Lledós, A.; Cucurull-Sánchez, L.; Novoa, J. J.; Alvarez, S.; Tolman, W. B. *Inorg. Chem.* **2000**, *39*, 4059.

picture of Cu–O bonding in the  $\text{Cu}_2\text{O}_2$  diamond core structure and permitted significant insight into electronic structure contributions to the reactivities of these complexes. In the present study we have employed a combined spectroscopic/computational approach to obtain insight into the geometric and electronic structures of the  $\text{Ni}_2\text{O}_2$  core in  $[(\text{PhTt}^{\text{Bu}})_2\text{Ni}_2(\mu\text{-O})_2]$  **1**. Below, these results are compared to relevant data reported for bis- $\mu$ -oxo ( $\text{Cu}^{3+}$ )<sub>2</sub> complexes. To evaluate the influence of the thioether supporting ligands in **1**, we also compare Ni–O bonding in **1** and bis- $\mu$ -oxo ( $\text{Ni}^{3+}$ )<sub>2</sub> dimers that possess nitrogen supporting ligands.

#### 4.1. Influence of the Thioether Ligands on Ni–O Bonding.

In **1** the lowest-energy  $\text{O} \rightarrow \text{Ni}$  CT transition occurs at 17 700  $\text{cm}^{-1}$ , red-shifted by  $\sim 7000 \text{ cm}^{-1}$  as compared to the corresponding transition in bis- $\mu$ -oxo ( $\text{Ni}^{3+}$ )<sub>2</sub> dimers with nitrogen supporting ligands.<sup>5–7</sup> As the energies of CT transitions relate to metal–ligand bonding, this striking difference suggests that the supporting ligands have a crucial impact on  $\text{Ni}_2\text{O}_2$  core electronics in bis- $\mu$ -oxo ( $\text{Ni}^{3+}$ )<sub>2</sub> dimers.

Quantitative insight into the Ni–O bond strength can be obtained from rR experiments in conjunction with a normal coordinate analysis of the  $\text{Ni}_2\text{O}_2$  core vibrations. Itoh et al. reported rR data for several bis- $\mu$ -oxo ( $\text{Ni}^{3+}$ )<sub>2</sub> dimers with tridentate nitrogen donor ligands.<sup>7</sup> Depending on the specific donor ligand, the Ni–O breathing mode was observed in the range of 599–612  $\text{cm}^{-1}$  upon excitation in resonance with the  $\text{O} \rightarrow \text{Ni}$  CT absorption band at 24 400  $\text{cm}^{-1}$ . These values are consistently higher than the value of 590  $\text{cm}^{-1}$  for **1**. To verify whether this difference reflects stronger Ni–O bonds in the dimers with nitrogen ligands than in **1**, we performed a normal coordinate analysis on the former using the same force field as for **1** (see section 3.3.A) and an idealized  $D_{2h}$  core structure with Ni–O = 1.86 Å and Ni...Ni = 2.88 Å.<sup>69</sup> Using  $\nu(\text{Ni}-^{16}\text{O})$  of 612 and 599  $\text{cm}^{-1}$ , the respective upper and lower limits observed experimentally in ref 7, we obtain Ni–O stretch force constants of 2.85 and 2.73  $\text{mdyn}/\text{\AA}$ , respectively. These values are significantly higher than  $k_{\text{Ni-O}} = 2.64 \text{ mdyn}/\text{\AA}$  in **1**, thus indeed reflecting stronger Ni–O bonds in the dimers with nitrogen ligands.

To explain the electronic origin of this difference in Ni–O bond stretch, DFT computations were performed on an approximate model<sup>70</sup> of the crystallographically characterized complex  $[(\text{Tp}^{\text{Me}_3})_2\text{Ni}_2(\mu\text{-O})_2]$  (**4**),<sup>5</sup> a representative bis- $\mu$ -oxo ( $\text{Ni}^{3+}$ )<sub>2</sub> dimer with a tridentate nitrogen supporting ligand on each Ni center (Chart 1 shows the inner coordination sphere).<sup>18</sup> Analysis of the MO compositions of the three lowest unoccupied MOs (Table S8) obtained from a DFT calculation on **4** in the BS ( $M_s = 0$ ) state<sup>55</sup> provides detailed insight into the Ni–O bonding interactions in this species. Similar to **1**, the dominant Ni–O bonding interactions in **4** also involve the  $\text{Ni}1(xy), \alpha$  and  $\text{Ni}1(xy), \beta$  MOs, which are  $\sigma$  antibonding, and the  $\text{Ni}1(xz), \alpha$  MO, which is  $\pi$  antibonding with respect to the Ni–O bonds.<sup>71</sup> Importantly, the relative contributions of ligand orbitals to these

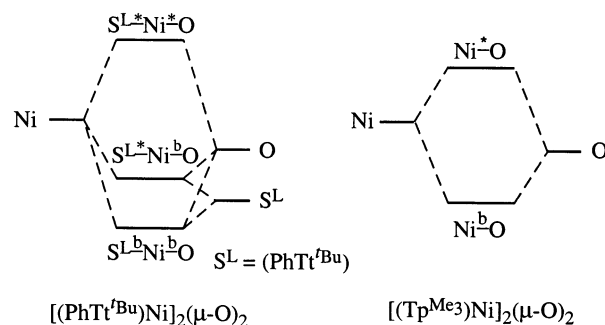


**Figure 8.** Schematic illustration of the influence of the sulfur 3p-derived thioether ligand orbitals of  $(\text{PhTt}^{\text{Bu}})$  on the Ni–O bonding interactions in  $[(\text{PhTt}^{\text{Bu}})_2\text{Ni}_2(\mu\text{-O})_2]$ .<sup>72</sup> For comparison the situation for  $[(\text{Tp}^{\text{Me}_3})_2\text{Ni}_2(\mu\text{-O})_2]$  is shown on the right. The b and asterisk symbols indicate the bonding and antibonding character of the corresponding bonds.

three MOs are significantly different for **1** and **4** (Tables 4 and S8, respectively). The sum of atomic orbital contributions to the three MOs are 131% Ni 3d, 85% O 2p, and 48% S 3p in **1** and 147% Ni 3d, 93% O 2p, and 16% N 2p in **4**. Thus, while in **4** these MOs possess only little N ligand orbital character, in **1** they carry substantial contributions from the sulfur 3p-derived thioether ligand orbitals. Consequently, the Ni–O bonds in **1** are less covalent (i.e., more ionic) in **1** than in **4**. This rather qualitative analysis is supported by a 4% lower average computed Ni–O bond order in **1** than in **4** (Figure S1), in excellent agreement with the 3–7% decrease in the Ni–O stretch force constant in **1** as compared to ( $\text{Ni}^{3+}$ )<sub>2</sub> dimers with nitrogen ligands (vide supra). DFT computations thus corroborate our conclusion drawn from rR data.

The large admixture of thioether sulfur p orbital character to the Ni–O bonding MOs also substantially affects the energies of the  $\text{Ni}_2\text{O}_2$  core MOs as shown schematically in Figure 8 (left).<sup>72</sup> In **1** the  $\text{Ni}_2\text{O}_2$  core orbitals strongly interact with the energetically close sulfur 3p-based thioether orbitals, leading to a bonding ( $\text{SL}^{\text{b}}\text{-Ni}^{\text{b}}\text{-O}$ ) and an antibonding ( $\text{SL}^*\text{-Ni}^*\text{-O}$ ) set of MOs with respect to the Ni–S bonds.<sup>73</sup> As the ( $\text{SL}^*\text{-Ni}^*\text{-O}$ ) set is derived from the oxo 2p orbitals, its electron density is predominantly localized along the Ni–O bonds. Consequently, MOs in this set serve as donors for  $\text{O} \rightarrow \text{Ni}$  CT transitions to the all-antibonding ( $\text{SL}^*\text{-Ni}^*\text{-O}$ ) Ni d-based set of MOs. As the latter are considerably less interacting with sulfur p orbitals than the former, the  $\text{O} \rightarrow \text{Ni}$  CT transition energies are reduced. Alternatively, in **4** the Ni–O bonding MOs ( $\text{Ni}^{\text{b}}\text{-O}$  in Figure 8, right) are essentially unperturbed by nitrogen 2p orbitals, resulting in higher  $\text{O} \rightarrow \text{Ni}$  CT transition energies than for **1**.

In conclusion, the presence of the thioether supporting ligands in **1** leads to a relatively low covalency of the Ni–O bonds and an unusually low  $\text{O} \rightarrow \text{Ni}$  CT transition energy. Thus, as compared to the N donor ligands present in all other bis- $\mu$ -oxo ( $\text{Ni}^{3+}$ )<sub>2</sub> dimers reported to date, the thioether ligand has a considerably greater influence on the frontier MOs. This unique property of the thioether ligand likely contributes to the reactivity of the Ni center in the precursor  $[(\text{PhTt}^{\text{Bu}})\text{NiCO}]$  toward  $\text{O}_2$ .

(69) As no crystallographic data are available for the complexes reported in ref 7, this molecular geometry is based on the crystal structure of **4**,<sup>5</sup> which has similar supporting ligands.  $k_{\text{O}}$  and  $k_{\text{O}_2}$  were fixed at 0.20  $\text{mdyn}/\text{\AA}/\text{rad}^2$  and 0.05  $\text{mdyn}/\text{\AA}$ , respectively, the same values used for **1**.

(70) In the model the methyl groups at the pyrazolyl rings were replaced by hydrogen atoms.

(71) The large contributions from Ni yz orbitals to the  $\text{Ni}1(xz), \alpha$  MO in **1** are replaced by contributions from the Ni  $z^2$  orbitals in **4**, reflecting the differences in coordination geometry at the Ni sites in **1** and **4**.

(72) The energetic ordering of the ligand-derived O (oxo) and S (thioether) ligand orbitals in **1** is based on the experimental observation that the  $\text{O}(\text{oxo}) \rightarrow \text{Ni}$  CT transition is considerably lower in energy than the S (thioether)  $\rightarrow \text{Ni}$  CT transitions (Figure 4).

(73) The b and asterisk symbols indicate the bonding and antibonding character of the corresponding bonds.



**4.2. Ni–O versus Cu–O Bonding.** Several theoretical studies performed on  $[(\text{NH}_3)_x\text{Cu}_2(\mu\text{-O})_2]^{2+}$  ( $x = 4, 6$ ) model complexes have provided a detailed description of Cu–O bonding in bis- $\mu$ -oxo ( $\text{Cu}^{3+}$ )<sub>2</sub> dimers.<sup>2,25,65,67</sup> Comparison of the results from these studies with our findings for **1** reveals that the dominant metal–oxo bonding interactions in the ( $\text{Ni}^{3+}$ )<sub>2</sub> and ( $\text{Cu}^{3+}$ )<sub>2</sub> dimers are very similar: they involve the metal  $xy$ -based MOs ( $\text{Ni}1(xy), \alpha$  and  $\text{Ni}1(xy), \beta$  in **1**) that have substantial contributions from oxo  $p_x$  and  $p_y$  orbitals, respectively, and are  $\sigma$  antibonding with respect to the metal–oxo bond. In **1**, the unoccupied  $\text{Ni}1(xz), \alpha$  MO that is  $\pi$  antibonding with respect to the Ni–O bond further contributes to Ni–O bonding. In contrast, because of the additional electron in  $\text{Cu}^{3+}$  ( $d^8$ ) as compared to  $\text{Ni}^{3+}$  ( $d^7$ ), the analogous MO in Cu is fully occupied and thus does not contribute to Cu–O bonding, lowering the bond order in  $\text{Cu}^{3+}$  ( $d^8$ ) as compared to  $\text{Ni}^{3+}$ . On the basis of this argument, the total strength of metal–oxo bonding would be expected to be slightly reduced in ( $\text{Cu}^{3+}$ )<sub>2</sub> relative to ( $\text{Ni}^{3+}$ )<sub>2</sub> dimers. However, the effective nuclear charge of  $\text{Ni}^{3+}$  ( $Z_{\text{eff}} = 7.55$ ) is slightly lower than that of  $\text{Cu}^{3+}$  ( $Z_{\text{eff}} = 8.20$ ).<sup>74</sup> Thus, the metal 3d orbitals are higher in energy for  $\text{Ni}^{3+}$  than for  $\text{Cu}^{3+}$ , leading to less covalent metal–oxo bonds. As this difference in covalency compensates for the differences in bond order, metal–oxo bonds are expected to be similarly strong in ( $\text{Ni}^{3+}$ )<sub>2</sub> and ( $\text{Cu}^{3+}$ )<sub>2</sub> dimers.

Henson et al.<sup>25</sup> reported a value of  $k_{\text{Cu-O}} = 2.70$  mdyn/Å for the force constant of the totally symmetric Cu–O stretching mode in  $[(\text{Me}_2\text{Et}_2\text{chd})_2\text{Cu}_2(\mu\text{-O})_2]^{2+}$  (**3**).<sup>18</sup> As the values of the fitted force constants depend on the specific force field chosen, we have redetermined  $k_{\text{Cu-O}}$  for **3** using the same force field as for **1** (section 3.3.A). The value obtained,  $k_{\text{Cu-O}} = 2.82\text{--}2.90$  mdyn/Å, is significantly higher than  $k_{\text{Ni-O}} = 2.64$  mdyn/Å determined for **1**, indicating substantially stronger metal–oxo bonds in **3**. However, as pointed out above, the nature of the supporting ligands in the Ni dimers strongly affects Ni–O bonding; for the complexes with nitrogen supporting ligands,  $k_{\text{Ni-O}}$  lies in the range of 2.73–2.85 mdyn/Å, virtually identical to  $k_{\text{Cu-O}} = 2.82\text{--}2.90$  mdyn/Å obtained for **3**. Furthermore, the frequency of the Cu–O stretching mode that mirrors the Cu–O bond strength has been reported to vary substantially between 583 and 616  $\text{cm}^{-1}$  for a variety of bis- $\mu$ -oxo ( $\text{Cu}^{3+}$ )<sub>2</sub> dimers with different nitrogen supporting ligands.<sup>44</sup> Thus, the Cu–O bond strength depends on ligand influences such as steric strain and the coordination number at the Cu site. Overall it appears that the metal–oxo bonds in bis- $\mu$ -oxo ( $\text{Ni}^{3+}$ )<sub>2</sub> and ( $\text{Cu}^{3+}$ )<sub>2</sub> dimers are similarly strong for a given set of supporting ligands. A parallel rR study on bis- $\mu$ -oxo ( $\text{Ni}^{3+}$ )<sub>2</sub> and ( $\text{Cu}^{3+}$ )<sub>2</sub> dimers possessing identical supporting ligands should aid further in discriminating between metal and ligand contributions to differences in Cu–O and Ni–O bonding.

**4.3. Nature of Oxo→Metal CT Excitations in Ni<sub>2</sub> and Cu<sub>2</sub> Dimers.** In bis- $\mu$ -oxo ( $\text{Ni}^{3+}$ )<sub>2</sub> and ( $\text{Cu}^{3+}$ )<sub>2</sub> dimers the lowest-energy intense absorption bands are due to oxo→metal CT transitions whose energies depend on the extent of covalency in metal–oxo bonds. On the basis of our computations for **1** (section 4.2) and published data for **3**,<sup>25</sup> this covalency is comparable in ( $\text{Ni}^{3+}$ )<sub>2</sub> and ( $\text{Cu}^{3+}$ )<sub>2</sub> dimers that both possess nitrogen supporting ligands. As the oxo→metal CT transitions

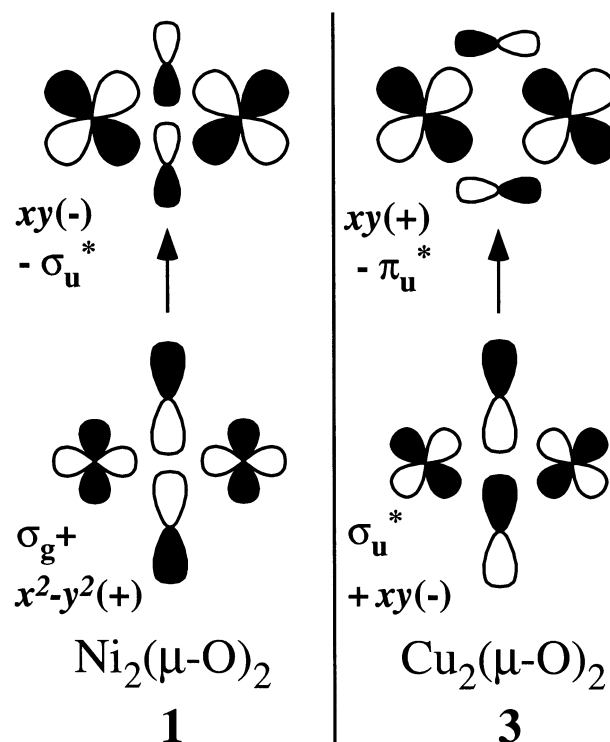


**Figure 9.** Schematic representation of the relevant donor and acceptor MOs for the oxo→metal CT transitions in  $[(\text{PhTr}^{\text{Bu}})_2\text{Ni}_2(\mu\text{-O})_2]$  (**1**) and a representative bis- $\mu$ -oxo ( $\text{Cu}^{3+}$ )<sub>2</sub> dimer.

in these dimers are invariably observed near 25 000  $\text{cm}^{-1}$  for both ( $\text{Ni}^{3+}$ )<sub>2</sub> and ( $\text{Cu}^{3+}$ )<sub>2</sub> complexes,<sup>5–7,25</sup> it is interesting to explore whether they involve the same donor and acceptor MOs in each dimer.

Experimental insight into the nature of oxo→metal CT transitions can be obtained from an analysis of the geometric distortions of the  $\text{M}_2\text{O}_2$  core in the corresponding excited states. Excited-state distortions for the bis- $\mu$ -oxo ( $\text{Cu}^{3+}$ )<sub>2</sub> dimer  $[(\text{Me}_2\text{Et}_2\text{chd})_2\text{Cu}_2(\mu\text{-O})_2]^{2+}$  (**3**) were previously determined from rR data in conjunction with a normal coordinate analysis of the  $\text{Cu}_2\text{O}_2$  core vibrations.<sup>25</sup> Upon O→Cu CT excitation, the Cu–O bonds were found to elongate significantly from 1.80 to 1.89 Å. Importantly, this change is accompanied by a drastic decrease in O⋯O separation from 2.33 to 2.03 Å and an increase in Cu⋯Cu distance from 2.73 to 3.18 Å. These results indicate that upon O→Cu CT excitation the  $\text{Cu}_2\text{O}_2$  core is distorted toward a geometry known for  $\mu\text{-}\eta^2\text{:}\eta^2$  side-on peroxo bridged ( $\text{Cu}^{2+}$ )<sub>2</sub> dimers.<sup>75</sup> Alternatively, upon O→Ni CT excitation in **1** the Ni–O bond lengths are only moderately enlarged from 1.82 to 1.87 Å (section 3.4.B and Table 7). Importantly, the O⋯O separation remains virtually unchanged ( $-0.005$  Å), while the Ni⋯Ni distance is moderately enlarged from 2.83 to 2.92 Å.

This strikingly different behavior can be understood in terms of the different compositions of the donor and acceptor MOs involved in the oxo→metal CT excitations. The donor and acceptor MOs for the relevant O→Cu CT transition in **3**, obtained by Henson et al. from SCF-X $\alpha$ -SW calculations, are shown schematically in Figure 9 (right).<sup>25</sup> In **3** the donor MO is derived from the antisymmetric combination of the oxo  $p_y$

(74) Slater, J. C. *Quantum Theory of Atomic Structure*; McGraw-Hill: York, PA, 1960; Vol. 1, p 112.

(75) Typical geometry of  $\mu\text{-}\eta^2\text{:}\eta^2$  side-on peroxo bridged ( $\text{Cu}^{2+}$ )<sub>2</sub> dimers: Cu–O = 1.92 Å, O–O = 1.41 Å, and Cu⋯Cu = 3.56 Å. See ref 25.

orbitals referred to as  $\sigma_u^*$ .<sup>76</sup> This MO, which exhibits substantial contributions from the Cu  $xy$  orbitals, is  $\sigma$  bonding with respect to the Cu–O bonds and is  $\sigma$  antibonding with respect to the O $\cdots$ O bond vector. Alternatively, the acceptor MO, labeled  $xy(-) - \pi_u^*$ , is  $\sigma$  antibonding with respect to Cu–O bonds but only weakly  $\pi$  antibonding with respect to the O $\cdots$ O bond vector. Hence, upon O $\rightarrow$ Cu CT excitation an electron is formally promoted from an O $\cdots$ O  $\sigma$  antibonding MO to a Cu–O  $\sigma$  antibonding MO, leading to partial O–O bond formation at the expense of the Cu–O bond strength. These changes in bonding lead to the large changes in O $\cdots$ O, Cu $\cdots$ Cu, and Cu–O separations observed experimentally.

As shown in section 3.4.A, the situation is significantly different for **1**. In this complex the donor MO ( $27a_g$ ) is composed of the symmetric (+) combination of the Ni  $x^2-y^2$  orbitals and the oxo  $p_y$  orbitals (Figure 9, left). This MO is  $\sigma$  bonding with respect to the O $\cdots$ O bond vector ( $\sigma_g$ ). The acceptor MO ( $29b_u$ ) is  $\sigma$  antibonding with respect to both the Ni–O bonds and the O $\cdots$ O bond vector. Hence, upon O $\rightarrow$ Ni CT excitation an electron is formally transferred from a Ni–O  $\sigma$  bonding to a Ni–O  $\sigma$  antibonding MO, leading to a weakening of the Ni–O bonds consistent with the observed Ni–O bond elongation. Importantly, as the electron is transferred from a  $\sigma$  bonding MO to a  $\sigma$  antibonding MO with respect to the O $\cdots$ O bond vector, no decrease in O $\cdots$ O separation is expected, which is in agreement with the experiment.

Comparison of the MO compositions for **1** and **4** shows that the donor and acceptor MOs are largely unaffected upon substitution of the thioether ligand by a nitrogen supporting ligand. We therefore conclude that despite very similar oxo $\rightarrow$ metal CT transition energies for  $(\text{Ni}^{3+})_2$  and  $(\text{Cu}^{3+})_2$  dimers possessing nitrogen ligands, the corresponding excitations are very different in nature because of differences in  $\text{M}_2\text{O}_2$  core electronics.<sup>77</sup> To explore whether these differences in  $\text{M}_2\text{O}_2$  core electronics relate to differences in reactivities of  $(\text{Ni}^{3+})_2$  and  $(\text{Cu}^{3+})_2$  dimers, the reaction coordinate for the side-on peroxo $\rightarrow$ bis- $\mu$ -oxo conversion of **1** is studied in the next section.

#### 4.4. $\mu\text{-}\eta^2\text{:}\eta^2$ Peroxo $\rightarrow$ Bis- $\mu$ -oxo $\text{M}_2\text{O}_2$ Core Conversion.

As the corresponding  $\mu\text{-}\eta^2\text{:}\eta^2$  side-on peroxo complex is presumably a transient reaction intermediate in the formation of  $[(\text{PhTt}^{\text{Bu}})_2\text{Ni}_2(\mu\text{-O})_2]$ , exploration of the reaction coordinate for the side-on peroxo $\rightarrow$ bis- $\mu$ -oxo conversion to yield **1** is of significant interest. For  $\text{Cu}_2$  dimers, both the side-on peroxo<sup>78,79</sup> and the bis- $\mu$ -oxo<sup>3</sup> core structures have been reported. Their relative stabilities, described in detail by Tolman and Que,<sup>1</sup> are strongly dependent on the supporting ligands, the polarity of the solvent, the temperature, and the identity of the counterions. With  $^{\text{iPr}}\text{TACN}^{15,18}$  and several other supporting ligands,<sup>20–24</sup> both the side-on peroxo and the bis- $\mu$ -oxo isomers coexist, thus providing experimental evidence that these particular isomers participate in a chemical equilibrium. Alternatively, only bis-

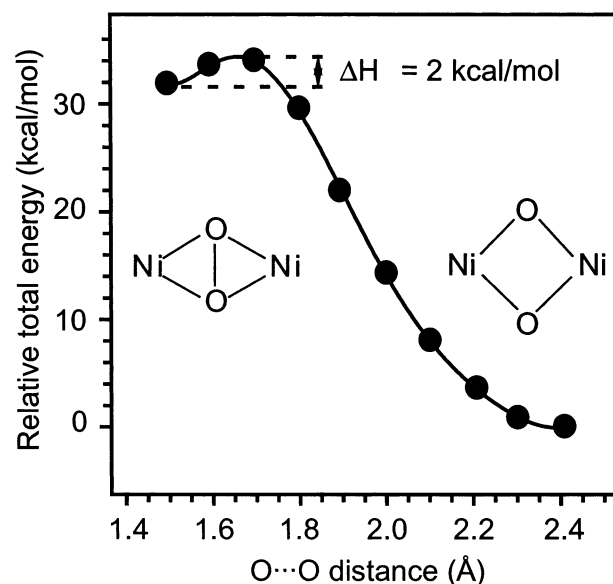


**Figure 10.** Variation of the relative total energy upon conversion of the hypothetical model of the side-on peroxo  $[(\text{PhTt}^{\text{Bu}})_2\text{Ni}_2(\mu\text{-}\eta^2\text{:}\eta^2\text{-O}_2)]$  species **2** to the bis- $\mu$ -oxo  $[(\text{PhTt}^{\text{Bu}})_2\text{Ni}_2(\mu\text{-O})_2]$  dimer model **1** obtained from a series of DFT geometry optimizations with constrained O $\cdots$ O distances.

$\mu$ -oxo  $(\text{Ni}^{3+})_2$  complexes have been reported to date,<sup>5–7,19</sup> indicating that they are significantly stabilized relative to their putative side-on peroxo precursors. Factors contributing to this difference in relative stabilities of  $\text{Cu}_2$  and  $\text{Ni}_2$  dimers are largely unknown.

To explore the reaction coordinate for the side-on peroxo $\rightarrow$ bis- $\mu$ -oxo conversion to yield **1**, a series of DFT computations were performed. In a first step, the molecular structure of an approximate model<sup>80</sup> of the hypothetical  $\mu\text{-}\eta^2\text{:}\eta^2$  side-on peroxo-bridged  $(\text{Ni}^{2+})_2$  dimer,  $[(\text{PhTt}^{\text{Bu}})_2\text{Ni}_2(\mu\text{-}\eta^2\text{:}\eta^2\text{-O}_2)]$  (**2**), was obtained from a symmetry-unrestricted DFT geometry optimization in the BS ( $M_S = 0$ ) state. The O–O bond length of 1.489 Å obtained for this model is consistent with a bridging peroxide moiety (atomic coordinates are listed in Table S5). Structures along a model reaction path converting **2** to **1** were generated next by varying the O–O distance in fixed increments of 0.101 Å from 1.489 to 2.407 Å while fully relaxing all other degrees of freedom.<sup>81</sup>

The change in total energy along the side-on peroxo **2** $\rightarrow$ bis- $\mu$ -oxo **1** reaction pathway (Figure 10) reveals a strong stabilization of **1** relative to **2** by 1.38 eV (32.0 kcal/mol) and a very low activation energy barrier of only 0.08 eV (2.0 kcal/mol). As these computations neglect solvation effects, **1** would be further stabilized relative to **2** in a polar solvent because of the increased polarity within the  $\text{Ni}_2\text{O}_2$  core. For  $\text{Cu}_2$  dimers in a medium with a dielectric constant of  $\epsilon = 10$ , this difference in solvation free energy has been calculated to be 5.6–8.4 kcal/mol in favor of the bis- $\mu$ -oxo core depending on the level of theory.<sup>65</sup> Thus, including solvation effects, **1** may be stabilized over **2** by as much as 40 kcal/mol.<sup>82</sup> As this value is much larger than the contribution from solvation, the equilibrium between

(76) Although there is no O–O bond in the bis- $\mu$ -oxo structure, the bonding and antibonding combinations of the oxygen p orbitals in the bis- $\mu$ -oxo dimers are referred to using the  $D_{\infty h}$  Mulliken symbols that are typically employed to label the  $\text{O}_2$ -derived MOs in side-on peroxo dimers.

(77) Therefore, it appears that the energetic coincidence of the oxo $\rightarrow$ metal CT transitions around  $25\,000\text{ cm}^{-1}$  for  $(\text{Ni}^{3+})_2$  and  $(\text{Cu}^{3+})_2$  dimers with similar ligands is most probably fortuitous.

(78) Kitajima, N.; Fujisawa, K.; Fujimoto, C.; Moro-oka, Y.; Hashimoto, S.; Kitagawa, T.; Toriumi, K.; Tatsumi, K.; Nakamura, A. *J. Am. Chem. Soc.* **1992**, *114*, 1277.

(79) Pidcock, E.; Obias, H. V.; Abe, M.; Liang, H.-C.; Karlin, K. D.; Solomon, E. I. *J. Am. Chem. Soc.* **1999**, *121*, 1299.

(80) Similar to our calculations on **1**, the phenyl and *tert*-butyl groups on the  $(\text{PhTt}^{\text{Bu}})$  ligands were substituted by methyl groups.

(81) As the difference in total energies of the side-on peroxo and bis- $\mu$ -oxo isomers is much larger than the exchange splitting, possible complications associated with determining the relative weights of the spin singlet and triplet contributions to the BS state can be ignored.

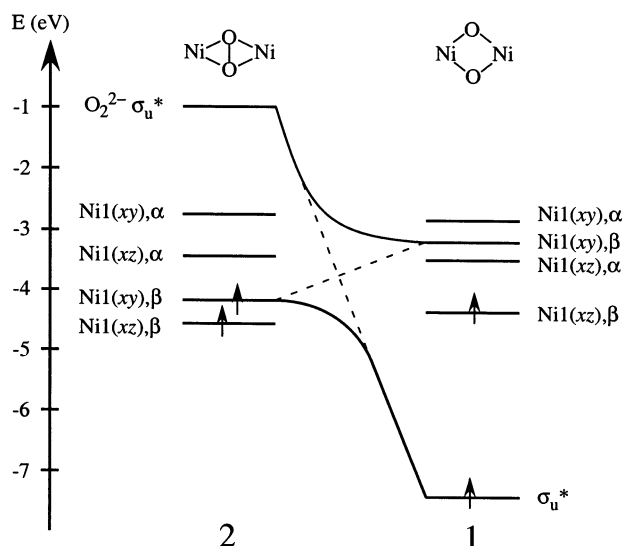


**Figure 11.** Walsh diagram correlating between key MOs of the hypothetical model of the side-on peroxo  $[(\text{PhTr}^{\text{Bu}})_2\text{Ni}_2(\mu\text{-}\eta^2\text{-}\eta^2\text{-O}_2)]$  species (**2**) and the bis- $\mu$ -oxo  $[(\text{PhTr}^{\text{Bu}})_2\text{Ni}_2(\mu\text{-O})_2]$  dimer model (**1**).

**1** and **2** is expected to be not substantially altered by changing the solvent, in sharp contrast to the situation for  $\text{Cu}_2$  dimers.

Several theoretical studies revealed that for  $\text{Cu}_2$  dimers with sterically nondemanding supporting ligands such as ammine the side-on peroxo and bis- $\mu$ -oxo core structures are virtually isoenergetic, while bulky substituents disfavoring close metal-metal distances stabilize the side-on peroxo structure.<sup>65–68</sup> Therefore, in the absence of bulky ligands that sterically stabilize the peroxo structure, the strong energetic stabilization of the bis- $\mu$ -oxo core structure (**1**) relative to the side-on peroxo core structure (**2**) can be generalized for  $\text{Ni}_2\text{O}_2$  dimers. This conclusion is supported by the experimental observation that complexes with identical supporting ligands adopt the side-on peroxo structure for  $\text{Cu}_2$  but adopt the bis- $\mu$ -oxo structure for  $\text{Ni}_2$ .<sup>7,83</sup> We conclude that the metal ion plays a crucial role in defining the  $\text{M}_2\text{O}_2$  core electronic structure such as to promote O–O bond cleavage in side-on peroxo complexes more easily for  $(\text{Ni}^{2+})_2$  than for  $(\text{Cu}^{2+})_2$  species.

The relative energies of side-on peroxo and bis- $\mu$ -oxo core structures are governed by two competing effects. First, the Coulomb repulsion between the positively charged metal ions leads to a favoring of the side-on peroxo structure in which the positive charges are formally reduced from  $\text{M}^{3+}$  to  $\text{M}^{2+}$  and separated further apart. However, the reduction in Coulomb repulsion because of the reduced effective nuclear charge in  $\text{Ni}^{2+/3+}$  as compared to  $\text{Cu}^{2+/3+}$  is likely to be compensated for by the decreased covalency of metal–oxo bonds in  $\text{Ni}_2$  relative to  $\text{Cu}_2$  dimers. The important contribution to the side-on peroxo/bis- $\mu$ -oxo energetics therefore comes from an electron correlation effect arising from a strong stabilization of the peroxo  $\sigma_u^*$ -based MO. This effect has been studied in detail by Henson et al. for  $\text{Cu}_2$  dimers.<sup>25</sup> A similar analysis for  $\text{Ni}_2$  dimers is presented in Figure 11, which shows a correlation diagram for

key MOs in the side-on peroxo **2** (left) and bis- $\mu$ -oxo **1** (right)  $\text{Ni}_2\text{O}_2$  core structures. This diagram was obtained from symmetry-unrestricted DFT geometry optimizations for **2** and **1** in their respective BS ( $M_S = 0$ ) states. In **2**, the unoccupied peroxo  $\sigma_u^*$ -based MO is located 3.167 eV above the HOMO, which is mainly composed of the Ni  $xy$ -based orbital (Figure 11). It should be noted that because of the overestimation of covalency by DFT methods, this energy gap might actually be even smaller, while  $\sigma$  back-bonding (vide infra) is probably underestimated in our calculation. As the two MOs possess the same symmetry,<sup>84</sup> they interact, which gives rise to  $\sigma$  back-donation of electron density from the Ni  $xy$  orbital to the peroxo  $\sigma_u^*$  orbital that is  $\sigma$  antibonding with respect to the O–O bond. With increasing O $\cdots$ O distance, the peroxo  $\sigma_u^*$ -based MO is stabilized through  $\sigma$  bonding interactions with the Ni  $xy$  orbitals and drops below the Ni  $xy$  derived MOs. In the bis- $\mu$ -oxo limiting structure **1**, the corresponding orbital is stabilized by 6.4 eV relative to the peroxo  $\sigma_u^*$ -based MO in **2**. This energetic stabilization of the  $\sigma_u^*$  orbital is the main contribution to the lower energy of **1** relative to **2**. The decreased effective nuclear charge of  $\text{Ni}^{2+}$  ( $Z_{\text{eff}} = 7.2$ ) as compared to  $\text{Cu}^{2+}$  ( $Z_{\text{eff}} = 7.85$ )<sup>74</sup> leads to substantially higher energies of the Ni d-based orbitals and thus to a smaller energy gap to the peroxo  $\sigma_u^*$  orbital in **2**. Consequently, the amount of metal  $xy \rightarrow$ peroxo  $\sigma_u^*$  charge donation is considerably higher in  $(\text{Ni}^{2+})_2$  dimers than in  $(\text{Cu}^{2+})_2$  dimers, suggesting that the former are more strongly activated for O–O bond cleavage.

In addition to the large thermodynamic driving force, the low energy barrier of  $\Delta H^\ddagger = 2.0$  kcal/mol also facilitates **2** $\rightarrow$ **1** conversion. This value is significantly lower than that of  $\Delta H^\ddagger \approx 8\text{--}9$  kcal/mol reported for similar  $\text{Cu}_2$  complexes on the basis of DFT computations.<sup>66</sup> In **2**, both the Ni  $xy$  and the  $xz$  orbitals are half-occupied (see Figure 11), consistent with a high-spin  $d^8$  electron configuration. Therefore, the electron in the  $\text{Ni}1(xy),\beta$  MO can readily delocalize into the peroxo  $\sigma_u^*$ -based MO upon **2** $\rightarrow$ **1** conversion as indicated by the lower solid line in Figure 11. This minimizes the reorganization energy for **2** $\rightarrow$ **1** conversion, thus contributing to the low calculated energy barrier. Furthermore, as the peroxo  $\sigma_u^*$  orbital drops below the metal  $xy$  orbital upon conversion, the barrier height depends on the magnitude of the resonance integral  $H_{AB}$  involving these two MOs at the transition state geometry corresponding to the crossing point of the broken lines in Figure 11. Because of the close energetic proximity of the metal  $xy$  and peroxo  $\sigma_u^*$  orbitals in the peroxo structure, this crossing point lies closer to the side-on peroxo limit in the  $\text{Ni}_2$  dimer (Figure 11) than in the  $\text{Cu}_2$  dimers. Thus, assuming similar values of  $H_{AB}$  for  $\text{Ni}_2$  and  $\text{Cu}_2$  dimers, the energy barrier is lower in the former. In conclusion, our calculations suggest that side-on peroxo $\rightarrow$ bis- $\mu$ -oxo conversion is significantly more favorable for  $\text{Ni}_2$  dimers than for  $\text{Cu}_2$  dimers because the thermodynamic driving force is larger and the energy barrier lower in the former case.

**4.5. Summary and Conclusions.** The spectroscopic and computational studies on  $[(\text{PhTr}^{\text{Bu}})_2\text{Ni}_2(\mu\text{-O})_2]$  reported here provide the first detailed description of the  $\text{Ni}_2\text{O}_2$  core electronic structure in bis- $\mu$ -oxo  $(\text{Ni}^{3+})_2$  dimers. The dominant O $\rightarrow$ Ni CT transition of  $[(\text{PhTr}^{\text{Bu}})_2\text{Ni}_2(\mu\text{-O})_2]$  observed at 17 700  $\text{cm}^{-1}$  is red-shifted by  $\sim 7000$   $\text{cm}^{-1}$  relative to the corresponding

(82) The calculated stabilization energy is probably slightly larger than the experimental value because of the truncation of the *tert*-butyl groups of **1** and **2** in our computational models; tridentate supporting ligands with sterically demanding substituents are expected to disfavor close metal-metal distances and thus to favor the side-on peroxo structure. See ref 1.  
(83) Itoh, S.; Kondo, T.; Komatsu, M.; Fukuzumi, S. *J. Am. Chem. Soc.* **1995**, *117*, 4714.

(84) In the approximate  $C_{2h}$  symmetry and the HS state they both transform as  $b_u$ .



transition in bis- $\mu$ -oxo ( $\text{Ni}^{3+}$ )<sub>2</sub> dimers with nitrogen supporting ligands. This red-shift along with a relatively low Ni–O bond strength are primarily due to the presence of the thioether ligands in  $[(\text{PhTt}^{\text{Bu}})_2\text{Ni}_2(\mu\text{-O})_2]$  that directly influence the characters of the  $\text{Ni}_2\text{O}_2$  core MOs. The reduced effective nuclear charge of  $\text{Ni}^{3+}$  as compared to  $\text{Cu}^{3+}$  substantially impacts the  $\text{M}_2\text{O}_2$  core electronics in several ways. First, the covalency of metal–oxo bonds is reduced, which leads to an increase in negative charge on the oxygen atoms, thus rendering ( $\text{Ni}^{3+}$ )<sub>2</sub> complexes potentially more reactive for C–H abstraction than their ( $\text{Cu}^{3+}$ )<sub>2</sub> analogues. Furthermore, the nature of the dominant oxo→metal CT transition is altered, as in bis- $\mu$ -oxo ( $\text{Ni}^{3+}$ )<sub>2</sub> dimers the  $\sigma_u^*$ -derived MO lies too low in energy relative to the metal d-based acceptor MOs to serve as the donor MO for O→Ni CT transitions in the visible spectral region. Finally, the equilibrium between the side-on peroxo and bis- $\mu$ -oxo core structures, which is roughly balanced for several  $\text{Cu}_2$  complexes, is strongly shifted toward the bis- $\mu$ -oxo core in  $\text{Ni}_2$  dimers, and the energy barrier for side-on peroxo→bis- $\mu$ -oxo conversion is even lower than for  $\text{Cu}_2$  dimers. As this preference of the bis- $\mu$ -oxo core in  $\text{Ni}_2$  dimers is due to electronic effects, the utilization of sterically demanding supporting ligands that resist close

Ni⋯Ni distance provides a logical and attractive approach to the preparation of the presently unknown  $\mu\text{-}\eta^2\text{:}\eta^2$  side-on peroxo-bridged ( $\text{Ni}^{2+}$ )<sub>2</sub> dimer.

**Acknowledgment.** We cordially thank Dr. Frank Neese, Max-Planck Institut Mülheim, Germany, for carrying out the ORCA computations. R.S. gratefully acknowledges a postdoctoral fellowship from the Swiss National Science Foundation. T.C.B. and R.S. thank the University of Wisconsin–Madison for generous support. C.G.R. acknowledges support from the NSF (CHE-9974628). This paper is dedicated to Prof. Hans U. Güdel from the University of Bern (Switzerland) in honor of his 60th birthday.

**Supporting Information Available:** Atomic coordinates of the optimized geometries of **1** (Tables S1–S4), **2** (Table S5), atomic coordinates from the crystal structure of **4** (Table S6), total energies and spin densities for **1** in the four different spin states (Table S7), compositions of the relevant MOs in **4** (Table S8), and Ni–ligand bond orders in **1** and **4** (Figure S1). This material is available free of charge via the Internet at <http://pubs.acs.org>.

JA027049K